Ore Geology Reviews 96 (2018) 13–27

Contents lists available at ScienceDirect

Ore Geology Reviews

journal homepage: www.elsevier.com/locate/oregeorev

Bulk geochemistry, sulfur isotope characteristics of the Yuhuang-1 hydrothermal field on the ultraslow-spreading Southwest Indian Ridge

Shili Liao[a,b], Chunhui Tao[a,b,*], Huaiming Li[a,b], Fernando J.A.S. Barriga[c], Jin Liang[a,b], Weifang Yang[a,b], Junyu Yu[a,d], Chuanwei Zhu[e]

[a] Second Institute of Oceanography, State Oceanic Administration, Hangzhou 310012, Zhejiang, China
[b] Key Laboratory of Submarine Geosciences, State Oceanic Administration, Hangzhou 310012, Zhejiang, China
[c] Departamento de Geologia, Faculdade de Ciências, Universidade de Lisboa, Lisboa, Portugal
[d] Ocean College, Zhejiang University, Zhoushan 316021, Zhejiang, China
[e] State Key Laboratory of Ore Deposit Geochemistry, Institute of Geochemistry, Chinese Academy of Sciences, Guiyang 550002, Guizhou, China

ARTICLE INFO

Keywords:
Bulk geochemistry
S isotopes
Yuhuang-1 hydrothermal field
Southwest Indian Ridge

ABSTRACT

The Yuhuang-1 hydrothermal field (HF) was discovered recently on the ultraslow-spreading Southwest Indian Ridge (segment 29). This field comprises two main sulfide deposition areas, including the southwest sulfide area (SWS) and the northeast sulfide area (NES), all of which are about 500 m in diameter. Sulfide-rich samples collected on the seafloor consist of zinc-rich, iron-rich, and silicified samples. The Zn-rich samples contain up to 60% sphalerite and 5% chalcopyrite, while iron-rich samples primarily contain pyrite and marcasite, and silicified sulfide rich samples primarily consist of amorphous silicon (70%), pyrite (15%–20%), and minor sphalerite. Sulfide rich samples generally show mound features with similar mineral assemblages, except that the NES contains pyrrhotite, indicating precipitation under relatively reduced conditions. Bulk geochemistry of the SWS and NES massive sulfide samples display similar Au, Co, Ni, and Si contents and Ni/Co ratios, similar to mafic-related HFs, while the Sn content and the Cd/Zn ratio are comparable to ultramafic-related HFs, which probably indicates a multi-stage origin. Sulfides rich samples from the SWS have $\delta^{34}S$ values ranging from −1.37‰ to 6.02‰ with a median value of 0.83‰. Currently, the $\delta^{34}S$ value of −1.37‰ is the lowest sulfur isotope composition observed in HFs on ultraslow-spreading ridges. Bacteria-derived sulfur, which is calculated to be 10%–25% of the total sulfur component, is likely the cause of the negative sulfur isotope composition. Conversely, the $\delta^{34}S$ values of the seafloor sulfides rich samples in the NES ranges from 3.75‰ to 8.73‰ with a median value of 4.74‰, which is distinctly heavier than that of the SWS. This study suggests that the SWS and NES of the Yuhuang-1 HF probably formed during different mineralization stages.

1. Introduction

Recent surveys have demonstrated that the ultraslow-spreading ridges, which are characterized by ultraslow-spreading rates and limited magma supply, also develop hydrothermal activity (Baker et al., 2004). Compared with fast- and superfast-spreading ridges, hydrothermal activity on slow and ultraslow-spreading ridges shows a longer history of fluid flow and larger tonnage of metals, which may contribute to approximately 86% of the total sulfide resources on mid-ocean ridges (MORs; Hannington et al., 2011). Currently, of the more than 140 confirmed hydrothermal fields with significant sulfide mineralization discovered on MORs (Beaulieu, 2015), only approximately 12 of them were discovered on ultraslow-spreading ridges, including Von Damm (Connelly et al., 2012) and Beebe (also known as Picard; Webber et al., 2015; German et al., 2010; Kinsey and German, 2013) on the Cayman Trough in the Caribbean; Aurora (Edmonds et al., 2003), Loki's Castle, and Jan Mayen on the Mohn's Ridge (Pedersen et al., 2010); and Mount Jourdanne (Nayak et al., 2014), Longqi-1 (Dragon Flag), Yuhuang-1, Duanqiao-1, Tiancheng-1, Tianzuo-1 and Changbai-1 (Tao et al., 2012, 2014; Yang et al., 2016) on the Southwest Indian Ridge (SWIR). The hydrothermal activities at these sites show diverse settings and mineralization. For example, the Beebe hydrothermal field (HF) is related to ridge axis volcanism (Kinsey and German, 2013), whereas the formation of the Von Damm Vent Field is controlled by oceanic core complexes (OCC; Connelly et al., 2012). The fluid in Loki's Castle is affected by sediments (Baumberger et al., 2016), while sulfide in Mount Jourdanne is rich in Pb (Nayak et al., 2014), which is the typical feature of back arc sulfides, and Changbai-1 is a carbonate field that likely has a

* Corresponding author at: Second Institute of Oceanography, State Oceanic Administration, Hangzhou 310012, Zhejiang, China.
E-mail address: taochunhuimail@163.com (C. Tao).

https://doi.org/10.1016/j.oregeorev.2018.04.007
Received 26 November 2017; Received in revised form 1 April 2018; Accepted 4 April 2018
Available online 05 April 2018
0169-1368/

similar genesis to the Lost City (Tao et al., 2014). However, compared to fast- and slow-spreading ridges, there are few studies focusing on hydrothermal systems in ultraslow-spreading ridges currently.

The SWIR is an ultraslow-spreading ridge (Dick et al., 2003). Previous studies have illustrated that the frequency of its hydrothermal activity development is significantly higher than that predicted by the traditional prediction model (German et al., 1998; Tao et al., 2012). Currently, about half of the confirmed HFs of ultraslow-spreading ridges are located on the SWIR (Tao et al., 2014), among which half of them are usually controlled by deep penetrating faults with deep fluid circulation (Tao et al., 2014). These hydrothermal fields generally have large size and several generations as a result of long time period fluid flow (Nayak et al., 2014). However, there have been limited studies of the hydrothermal activities on the SWIR. Moreover, the studies conducted so far have primarily focused on the Longqi-1 and Mount Jourdanne HFs (Tao et al., 2011; Ye et al., 2012; Nayak et al., 2014). To date, we still know little about sulfide mineralization on the ultraslow spreading ridges. Sulfide geochemistry and sulfur isotopic features are powerful methods to track element sources, migration processes, and physical and chemical conditions during mineralization processes (Peter and Shanks, 1992; Eiler et al., 2014). Here, we analyze bulk geochemistry and S isotope compositions of sulfide rich samples to investigate the source of ore-forming materials and sulfide mineralization process of the Yuhuang-1 HF on the SWIR.

2. Geological background

The SWIR separates the African and Antarctic Plates. It extends approximately 8000 km from the Bouvet Triple Junction in the west to the Rodrigues Triple Junction in the east. The SWIR is defined as an ultraslow-spreading MOR with a semi-spreading rate of approximately 0.7–0.9 cm/yr (Dick et al., 2003). This ridge is characterized by very rugged topography and an axial rift valley with water depths deeper than 5000 m and is cut by a series of north–south striking transform faults (Fig. 1a). Owing to the hotspots of Marion and Crozet in the southwest, this region shows strong negative residual mantle Bouguer gravity anomalies, indicating relatively active crust–mantle exchange and deep magmatism in this region, as well as a sufficient supply of magma and heat (Georgen et al., 2001; Sauter et al., 2001, 2009). These conditions are sufficient for the occurrence of seafloor hydrothermal activity and the formation of sulfide deposits. Even though the source of the magma supply on this ridge section is still controversial (Zhang et al., 2013; Zhou and Dick, 2013; Li et al., 2015), the strong magmatic activity and the intensity of the hydrothermal activity are obviously different from those of other ultraslow-spreading ridges (Tao et al., 2012).

The Yuhuang-1 HF was discovered on the 21st cruise by RV Dayangyihao in 2010 (Han et al., 2010). The field is located on the south rift wall of Segment 29 between the Indomed and Gallieni transform faults. This segment of the ridge shows asymmetric spreading features, and the ridge volcanic axis (RVA) is developed on the rift valley. The north ridge flank spreads normally and has developed a series of NEE-striking normal faults that form a graben terrain, which is undeveloped in the south ridge flank. This HF is located approximately 7.5 km from the ridge axis with a water depth ranging from 1400 to 1600 m (Han et al., 2010, 2015). The terrain where the field is located shows NEE-striking highland features, with an elevation of about 1500 m to the bottom of the rift valley (Fig. 1b and c). The NEE-striking highland has developed a series of NE–NWW-striking faults. Data from several cruises have revealed that calcareous sediments are distributed on the east side of the HF and that basalt and basaltic breccia are primarily distributed on the west side. In addition, the 21st and 40th cruises collected serpentinite by TV grab in the study area, suggesting that there are likely outcrops of ultrabasic rocks, which further implies the development of detachment fault.

Currently, two sulfide deposition areas have been discovered in this HF (Fig. 2): the southwest sulfide area (SWS) and the northeast sulfide area (NES). The SWS consists of discontinuous sulfide with a diameter about 500 m. Current sampling results show that the surface of this area primarily consists of sulfide rich accumulations with high content of sphalerite and amorphous silicon that without typical chimney structures (Table 1). Recent drilling at this area found that about 50 cm of the top of the drill core is primarily calcareous sediments, which is followed by sulfide rich samples that mainly compose of sphalerite and chalcopyrite, implying that there were high-temperature hydrothermal activities in the past. The NES, with a diameter of more than 500 m, is located approximately 600 m to the northeast of the SWS. Its surface primarily consists of discontinuously distributed sulfide rich accumulations and sulfide rich chimneys. The chimneys occur isolated on basalt without collapsed sulfide accumulations, similar to the occurrence of zinc chimneys on the EPR (Paradis et al., 1988). Active vents have not been discovered, suggesting that the hydrothermal activity has likely ceased.

3. Sampling and analysis methods

3.1. Mineralogy

Sulfide rich samples were firstly classified on hand specimen. Then, sections for mineralogy identification were prepared and observed at Key Laboratory of Submarine Geosciences, State Oceanic Administration under a Zeiss AXIO Scope.A1 microscope.

3.2. Microdrilling

In order to investigate sulfur isotope compositions of mineral grown belt of the sulfide rich samples, the microdrilling was carried out by a MICRODRILL SYSTEM at the State Key Laboratory of Ore Deposit Geochemistry, Institute of Geochemistry, Chinese Academy of Sciences. The diameter of the microdrill bit ranged from 0.2 to 2 mm, and a vacuum adsorption system was used to collect samples to ensure the purity of the samples. The specific parameters of this instrument and the sampling methods have previously been reported by Dong et al. (2013).

3.3. Sulfide rich samples chemistry

Major and trace elements were analyzed at the ALS Laboratory in Guangzhou, China. The samples were dried and crushed into 200 mesh. Subsequently, 250 μg of the ground powder samples were dissolved with $HClO_4$, HNO_3 and HF. The solutions were evaporated to dryness, and then the residue was leached and dissolved by diluted HCl. The trace elements Cu, Zn, Pb, Mn, Co, Ni, Cd, Mo, Ag, As, Cr, Ga, Sr, Sb, Se, Sn and Ba were analyzed via a POEMS III ICP-MS manufactured by Thermo Jarrell Ash Ltd., USA. The content of gold was analyzed by fire assaying. The major elements of SiO_2, Al_2O_3, TFe_2O_3, Na_2O, CaO, K_2O, MgO, TiO_2, P_2O_5 were analyzed by a PANalytical PW2424 X-ray fluorescence spectrometry. Analytical batches contained standard samples and 10% repeat samples, inserted to control the data accuracy. The test error of the data was within 5%.

3.4. Sulfur isotopes

The sulfur isotopes were analyzed using a Thermo Finnigan MAT 253 isotope ratio mass spectrometer (Thermo Scientific, Bremen, Germany) at the State Key Laboratory of Ore Deposit Geochemistry, Institute of Geochemistry, Chinese Academy of Sciences. The standard reference materials for the sulfur isotope measurement were IAEA-S-1, IAEA-S-2, and IAEA-S-3 (international measurement standards), which yielded a relative error (2σ) of < 0.15‰. All of the S isotope ratios are reported relative to Canyon Diablo Troilite.

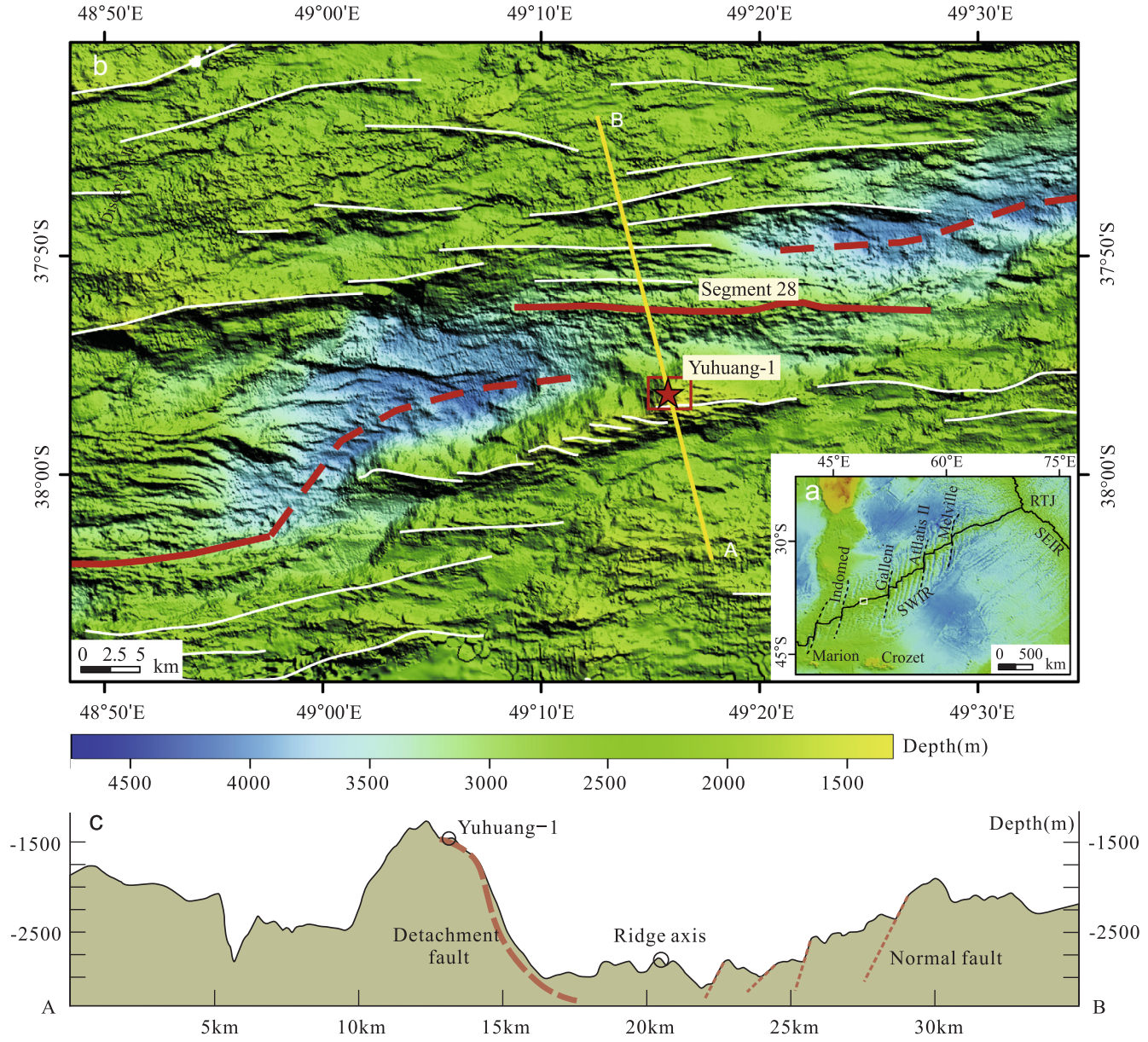

Fig. 1. (a) Geotectonic setting and (b) topography of the Yuhuang-1 HF. The red lines indicate the ridge axis; the white lines represent normal faults inferred from topography. The ridge segments and non-transform faults are based on Cannat et al. (1999) and Sauter et al. (2001). The topography is from multibeam sonar data. (For interpretation of the references to colour in this figure legend, the reader is referred to the web version of this article.)

4. Sulfide rich sample mineralogy

4.1. The SW sulfide area (SWS)

Three stations of sulfide rich samples weighted 496.5 kg were collected by TV-grab in the SWS. Four different mineralization types were identified by mineralogy and bulk geochemistry: a) sulfide-bearing veins in altered basalt; b) sphalerite-rich massive sulfide; c) pyritic massive sulfide; and d) silicified sulfide rich sample.

4.1.1. Sulfide-bearing veins in altered basalt (39II-TVG04)

The sample shows stockwork mineralization structures and has been intensely chloritized and silicified. Sulfide disseminations and veins (1–2 mm in width), primarily comprising pyrite and sphalerite, fill the altered basalt pores and fractures (Fig. 3a). The sulfide bearing veins occupy less than 10% of the volume of the sample. The mineral grain sizes are fine, generally with diameters of less than 0.1 mm. Pyrite occurs as anhedral to euhedral crystals and replaces sphalerite (Fig. 4a).

4.1.2. Sphalerite-rich massive sulfide (34II-TVG22-2)

This sample exhibit massive structures and consists of a pyrite crust and a sphalerite core. It is 10%–15% porous, and has a small fluid conduit in its inner part (Fig. 3b). It primarily consists of sphalerite (60%), pyrite (15%–20%), chalcopyrite (< 5%), marcasite (< 5%), isocubanite (< 5%), and amorphous silicon (15%–20%). Sphalerite grains adjacent to the conduit are coarser than distal ones, with grain sizes of up to 1 mm. Sphalerite shows two generations, where dark sphalerite (Sph1) was replaced by light sphalerite (Sph2), which commonly contains minor amounts of chalcopyrite, especially along the rims of the sphalerite grains (Fig. 4b). Pyrite occurs as rims in the sample and replaces sphalerite or is replaced by sphalerite, suggesting that the pyrite formed in two generations. Marcasite generally coexists with the pyrite.

4.1.3. Pyritic massive sulfide with a siliceous crust (34II-TVG22-7)

This sample mainly consists of two layers with different mineralogy (Fig. 3c). The outer part siliceous crust primarily comprises pyrite

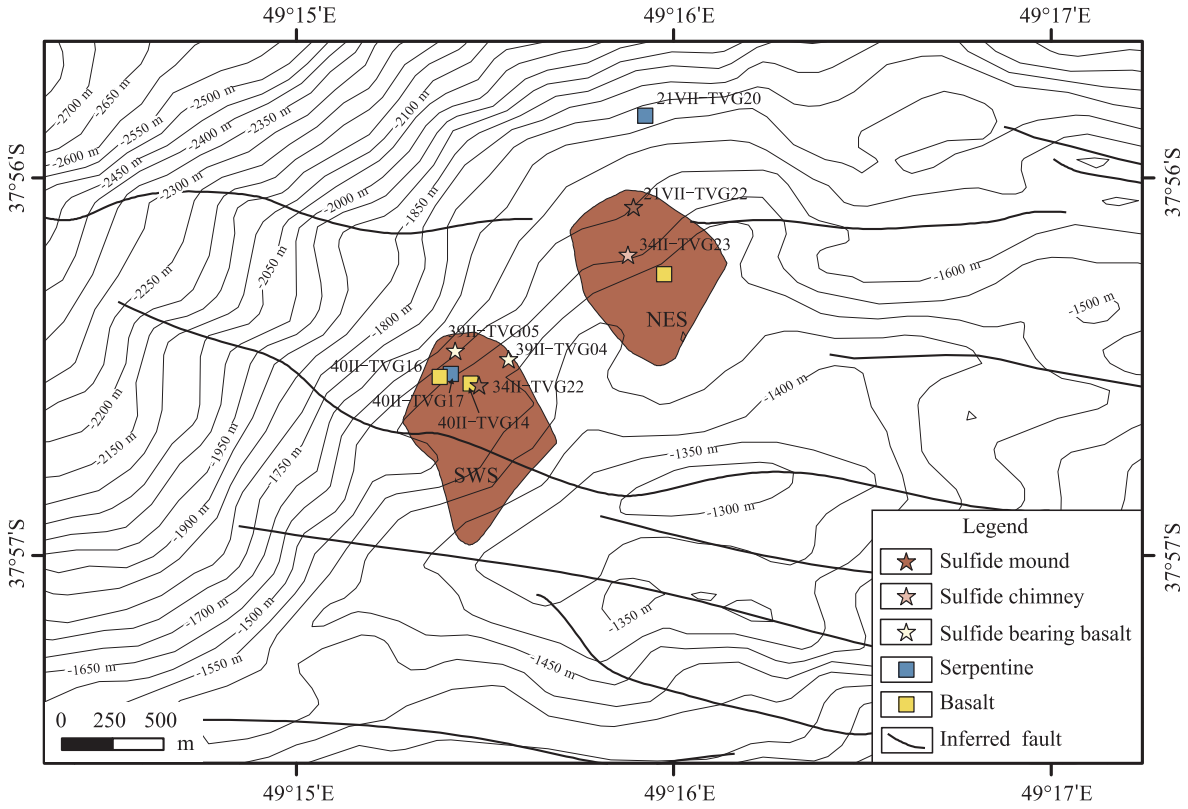

Fig. 2. Topography and geology of the Yuhuang-1 HF. The limits of NES and SWS were mapped through deep-tow observations. The samples were collected by TV-grab. The location of this area is shown in Fig. 1b.

Table 1
Sampling stations of sulfide rich samples, basalt and sediments in the Yuhuang-1 hydrothermal field.

Area	Station	Longitude (°E)	Latitude (°S)	Depth	Sampling equipment	Weight (kg)	Description
SWS	34II-TVG22	49.258	37.942	1499	TV-Grab	248.5	Sulfide rich breccia, oxide crusts, and hydrothermal sediments
	39II-TVG04	49.259	37.941	1622	TV-Grab	25	Sulfide bearing basalt, opal, and altered basalt
	39II-TVG05	49.257	37.941	1622	TV-Grab	75	Opal, hydrothermal Sediments, intensive altered basalt
	40II-TVG17	49.257	37.942	1539	TV-Grab	148	Ultramafic breccia, hydrothermal sediments
	40II-TVG14	49.258	37.942	1527	TV-Grab	101.5	Basalt
	40II-TVG16	49.256	37.942	1547	TV-Grab	23.8	Altered basalt
NES	21VII-TVG20	49.265	37.931	1698	TV-Grab	1	Basalt and serpentine
	21VII-TVG22	49.265	37.935	1443	TV-Grab	235	Sulfide rich sample and basalt
	34II-TVG23	49.265	37.937	1557	TV-Grab	72	Sulfide rich chimney, sulfide rich breccia, altered basalt
	34II-TVG24	49.266	37.938	1494	TV-Grab	35.2	Altered basalt breccia

(20%–30%), marcasite (10%), sphalerite (5%–10%), and amorphous Si (40–50%), whereas the inner part massive sulfide primarily contains pyrite and marcasite. Several fluid conduits with pyrite grown on the walls are observed. Sphalerite replaces pyrite and marcasite (Fig. 4c), implying that it formed at a later stage. The pyrite grains show euhedral to anhedral shapes and coexist with, or replace, marcasite (Fig. 4d).

4.1.4. Silicified sulfide rich sample

Three samples were selected for microscope observation (Fig. 3d–f), which showed marked similarity among the three. Sample 34II-TVG22-1 consists of two distinct sulfide rich breccia cemented by pyrite veins (Fig. 3d). Several fluid conduits are observed in both side of this sample. The left side primarily consists of amorphous silicon (70%), pyrite (15%–20%), and marcasite (5%), whereas the right side is more porous and primarily consists of amorphous silicon (60%), pyrite (15%–20%), sphalerite (10%–15%), marcasite (5%), and minor chalcopyrite. The pyrite grains usually show euhedral to anhedral shapes, and are partly replaced by sphalerite (Fig. 4e). The cemented pyrite veins generally show anhedral structures, and the mineral grain size increases from the outer edge to the center (Fig. 4f). Framboidal pyrites were also identified (Fig. 4g).

4.2. The NE sulfide area (NES)

In this area, two stations of sulfide rich samples weighted 305 kg in total were collected by TV grab, including sulfide rich accumulations (21VII-TVG22) and a silicified sulfide rich chimney (34II-TVG23-1).

4.2.1. Pyritic massive sulfide (21VII-TVG22)

This sample shows vague mineralization zonation that could be divided into three layers: (1) the outer part primarily consists of pyrite, marcasite, and sphalerite, (2) the middle part primarily comprises sphalerite and pyrite, and (3) the inner part mainly consists of chalcopyrite and sphalerite (Fig. 3g). It primarily consists of sphalerite (10%–15%), pyrite (20%–30%), chalcopyrite (5%–10%), marcasite (10%–15%), pyrrhotite (5%–10%), isocubanite (< 5%) and amorphous

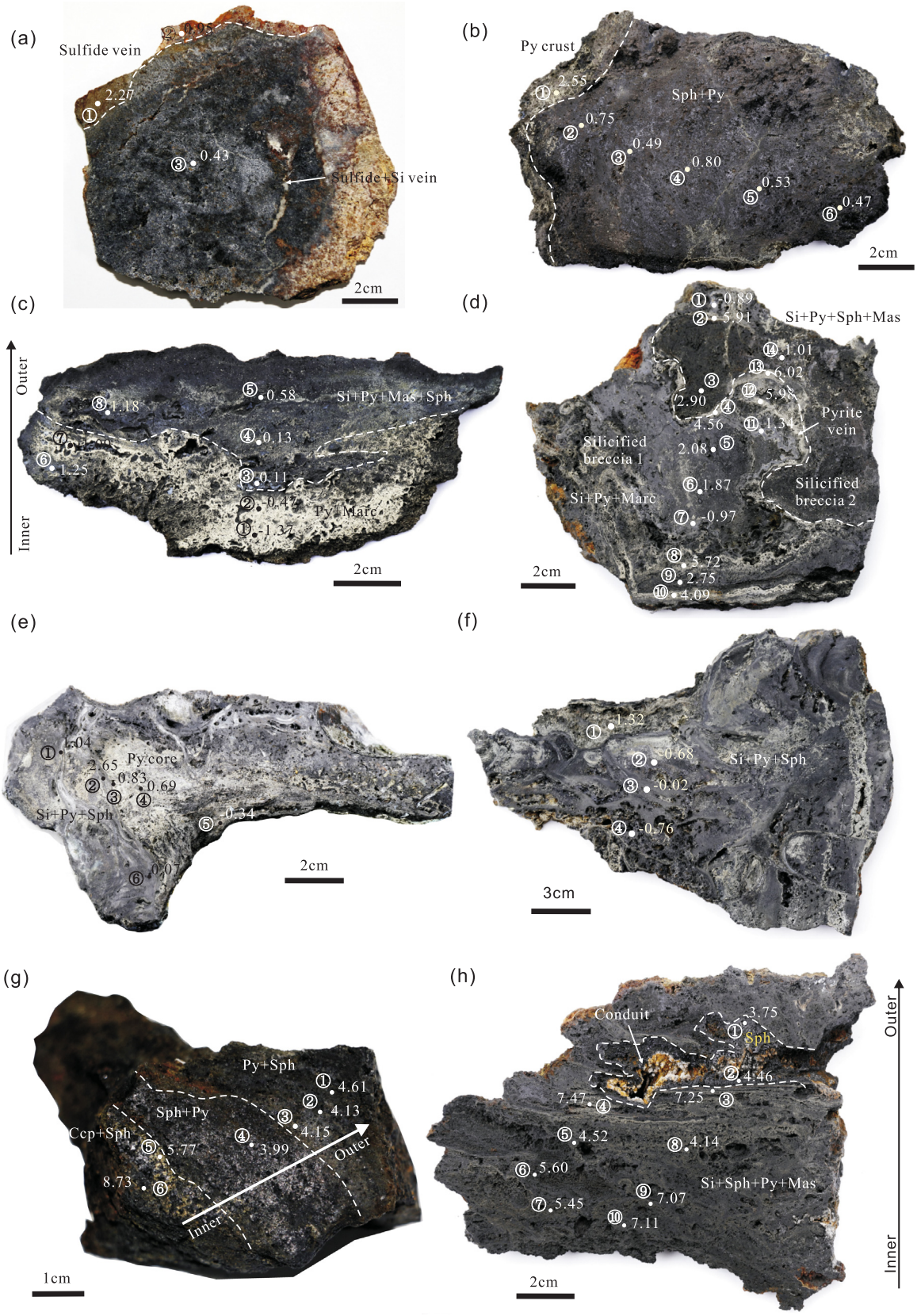

Fig. 3. Photographs of sulfide from the Yuhuang-1 HF. Samples (a)–(f) were collected from the SWS, whereas samples (g) and (h) were collected from the NES. (a) Sulfide-bearing veins in altered basalt; (b) Sphalerite-rich massive sulfide with a pyrite crust; (c) pyritic massive sulfide with a siliceous crust, primarily consisting of amorphous Si with pyrite on the top and pyrite at the bottom; the $\delta^{34}S$ values become heavier from the bottom to the top (see text); (d)–(f) silicified sulfide rich samples, sample (d) consists of two distinct silicified breccia cemented by pyrite veins, which show significantly heavier sulfur isotope composition; (g) pyritic massive sulfide with three layers; and (h) silicified chimney with a fluid conduit, sphalerites grown on the conduit walls show coarse crystals. White and dark dots mark the locations of the microdrilling samples. The numbers with circles indicate the microdrilling sample series for the sulfur isotope analysis corresponding to Table 3; the numbers adjacent to the circles indicate the corresponding sulfur analysis results.

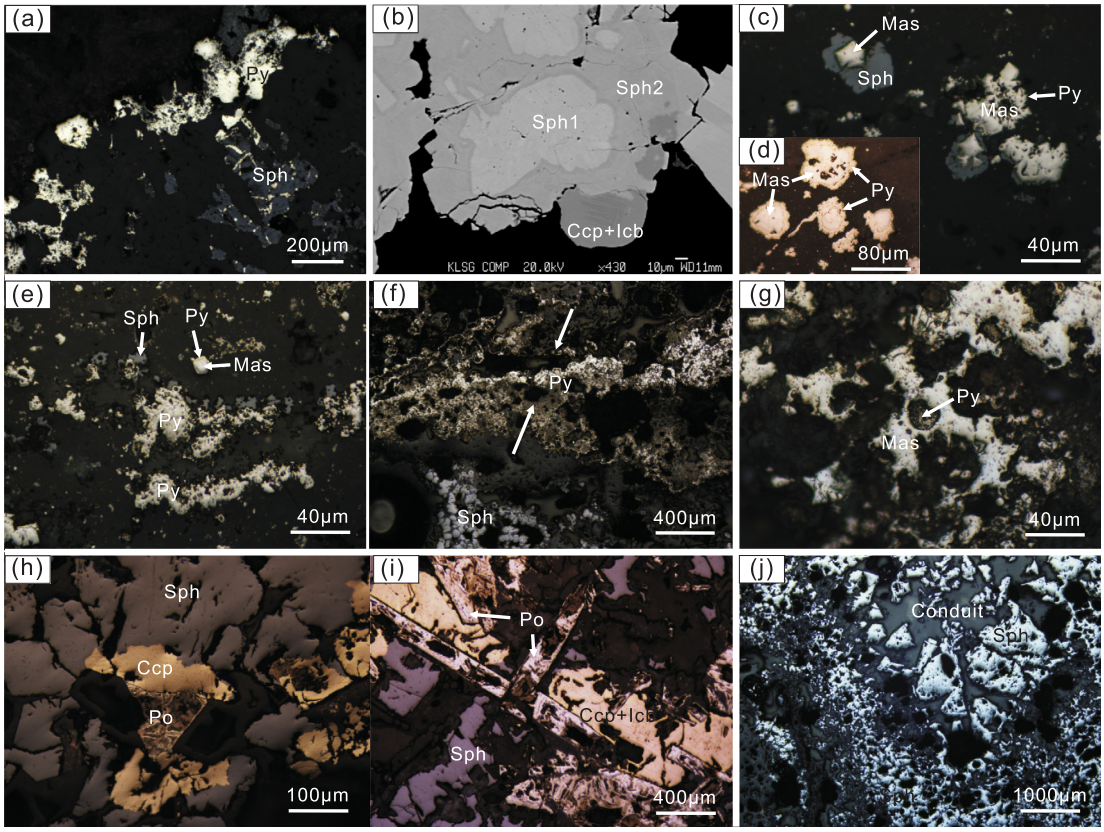

Fig. 4. Photomicrographs of sulfides in the Yuhuang-1 HF: (a) pyrite in the amorphous silica vein replacing sphalerite (39II-TVG04); (b) sphalerite shows two generations (Sph1 and Sph2) that replaced by chalcopyrite; the chalcopyrite shows a grid structure with isocubanite (34II-TVG22-2, EPMA photo); (c) marcasite replaced by pyrite in turn replaced by sphalerite (34II-TVG22-7); (d) euhedral marcasite shows pyrite growing edge (34II-TVG22-7); (e) marcasite replaced by pyrite (34II-TVG22-1), and then replaced by sphalerite; (f) pyrite vein in silicified sulfide; mineral grains in the inner part of the vein are larger, and the arrow shows the pyrite growth direction (34II-TVG22-1); (g) framboidal pyrite in marcasite (34II-TVG22-4); (h) sphalerite coexisting with chalcopyrite and replacing pyrrhotite (21VII-TVG22); (i) sphalerite and chalcopyrite showing grid structures with isocubanite, replacing euhedral pyrrhotite (21VII-TVG22); (j) sphalerite grains in the fluid conduit showing increasing diameters toward the conduit center (34II-TVG23-1). Mineral abbreviations: Ccp, chalcopyrite; Icb, isocubanite; Mas, marcasite; Po, pyrrhotite; Py, pyrite; and Sph, sphalerite.

silicon (10%). The pyrrhotite grains generally developed at layer (2) and (3) with euhedral structures and are partly replaced by sphalerite, which usually coexists with chalcopyrite (Fig. 4h and i).

4.2.2. Silicified sulfide rich chimney (34II-TVG23-1)

This sample was collected from the bottom part of a silicified chimney that grew on the basement basalt. The chimney is 1–2 m in height with no evidence of vent activity. This sample is porous, with multiple fluid conduits in which coarse sphalerite (Figs. 3h and 4j) and amorphous silicon developed. The chimney primarily consists of pyrite (5%–10%), sphalerite (20%–30%), marcasite (5%), and amorphous silicon (> 50%). Subhedral to anhedral pyrite grains occur with grain sizes from 2 to 8 μm and coexist with marcasite. Sphalerite grains usually replace pyrite and marcasite or are replaced by these minerals.

5. Results

5.1. Sulfide rich samples chemistry

In the samples from the SWS, the contents of Cu, Zn, and TFe ranged from 0.1 to 0.77 wt%, 0.00 to 39.77 wt%, and 5.26 to 38.33 wt%, respectively (Table 2). The trace elements Co, Ni, and Sn had values of 4.4–126.0, 3.0–16.3, and 0.2–137.0 ppm, respectively. The samples contained concentrations of gold ranging from 0.09 to 9.09 ppm with an average of 2.09 ppm. In the sulfide rich samples in the NES, the Cu, Zn, and Fe contents were 0.02–2.96, 0.11–45.44, and 6.80–44.48 wt%, respectively. The Co, Ni, and Sn contents were 21.6–1290.0, 1.3–6.5, and 0.2–205.0 ppm, respectively. The content of gold was < 0.02–4.73 ppm with an average of 1.37 ppm, which is similar to the sulfide rich samples in the SWS. The SiO_2 contents of the samples in the SWS and NES are relatively high, ranging from 10.25 to 74.86 wt% and from 5.44 to 75.70 wt%, respectively, showing that there are high abundances of amorphous silicon in the sulfide rich samples.

On the basis of the Cu, Fe, and Zn contents, the sulfide rich samples can be divided into iron-rich and zinc-rich samples (Fig. 5a), which is consistent with our detailed field and microscopy observations. According to the Fe, Zn, and Si contents, these sulfide rich samples can be divided into zinc-rich, iron-rich, and silicified samples (Fig. 5b). Overall, the sulfide rich samples in the SWS and NES had similar mineralization element contents. The zinc-rich samples have high Cd, Ag, Co, Sn, and Ga contents, whereas the silicified samples have lower amounts of trace elements than the zinc-rich and iron-rich samples.

5.2. Sulfur isotopes

5.2.1. Sulfide rich samples in the SWS

The $\delta^{34}S$ values of 41 microdrilling samples from the six sulfide rich samples range from −1.37‰ to 6.02‰ with a median value of 0.83‰ (Table 3). Sulfide veins in the altered basalt, sphalerite-rich massive sulfide, and pyritic massive sulfide show consistent $\delta^{34}S$ values that are close to zero, ranging from −1.37‰ to 2.55‰. The silicified sulfide rich samples have a larger distribution range of $\delta^{34}S$ (−0.97‰ to 6.02‰), in which the pyrite veins (4.09‰ to 6.02‰) have much higher $\delta^{34}S$ than that of the surrounding samples (−0.97‰ to 2.90‰;

Table 2
Bulk chemistry of sulfide rich samples in the Yuhuang-1 HF.

Elements		Au	SiO_2	Al_2O_3	Na_2O	CaO	K_2O	MgO	TiO_2	P_2O_5	TFe	S	LOI	Cu	Zn
Unit		μg/g	%	%	%	%	%	%	%	%	%	%	%	%	%
Detection limit		0.02	0.01	0.01	0.01	0.01	0.01	0.01	0.01	0.01	0.01	0.01	0.01	0.01	0.01
34II-TVG22-1–2	Fe-Rich massive sulfide	0.09	10.25	< 0.01	0.19	0.03	0.01	0.07	0.01	0.04	38.33	> 40	32.52	0.14	1.49
34II-TVG22-7	Fe-Rich massive sulfide	0.34	32.8	< 0.01	0.09	0.03	0.01	0.08	0.01	0.03	30.15	34.32	23.75	0.04	0.09
34II-TVG22-5	Fe-Rich massive sulfide	1.97	25.5	0.14	0.34	0.07	0.04	0.07	0.01	0.03	27.49	32.24	28.76	0.1	5.07
34II-TVG22-2	Zn-rich massive sulfide	9.09	10.7	0.11	0.44	0.07	0.03	0.06	0.01	0.02	12.8	29.28	18.58	0.77	39.77
34II-TVG22-1	Silicified sulfide rich sample	0.85	60.5	0.04	0.18	0.03	0.01	0.05	0.01	0.02	15.67	17.66	15.78	0.1	0.70
34II-TVG22-3	Silicified sulfide rich sample	1.03	57.8	0.11	0.4	0.05	0.03	0.08	0.01	0.02	13.18	16.18	16.67	0.11	4.43
34II-TVG22-4	Silicified sulfide rich sample	2.63	57.1	0.07	0.2	0.05	0.01	0.04	0.02	0.02	14.69	17.82	15.88	0.14	4.72
34II-TVG22-6	Silicified sulfide rich sample	0.71	65.1	0.04	0.22	0.08	0.01	0.07	0.01	0.02	12.87	14.54	14.32	0.22	1.26
39II-TVG04-2	stockwork		74.86	0.02	0.05	7.14	< 0.01	0.39	< 0.01	0.11	5.26	1.07	6.35	0.49	0.00
	Average of massive(4)	2.87	19.81	0.06	0.27	0.05	0.02	0.07	0.01	0.03	27.2	23.96	25.9	0.26	11.61
	Average of Total(9)	2.09	43.85	0.06	0.23	0.84	0.02	0.1	0.01	0.03	18.9	18.12	19.18	0.23	6.39
34II-TVG23-1H	Iron-rich sulfide chimney	0.24	18.15	0.03	0.15	0.09	0.05	0.18	0.01	0.04	44.48	13.12	15.22	0.09	1.94
21VII-TVG22-1	Iron-rich massive sulfide	2.97	13.05	0.02	0.24	0.05	0.02	0.08	0.02	0.03	29.24	33.92	33.88	2.65	5.73
21VII-TVG22-2	Zinc-rich massive sulfide	4.73	22.4	0.07	0.34	0.04	0.02	0.03	0.01	0.02	13.25	25.71	16.79	2.96	29.89
21VII-TVG22-A-3	Zinc-rich massive sulfide		5.44	< 0.01	0.32	0.03	0.02	0.16	< 0.01	< 0.01	11.8	30.6		2.49	45.44
34II-TVG23-1	Silicified sulfide chimney	0.02	75.7	0.06	0.16	0.06	0.01	0.05	0.01	0.01	8.74	9.13	11.3	0.05	0.85
34II-TVG23-3	Silicified sulfide chimney	0.28	65.3	0.08	0.2	0.23	0.01	0.1	0.01	0.02	7.66	11.65	10.24	0.08	10.00
34II-TVG23-4	Silicified sulfide chimney	< 0.02	72.8	0.05	0.15	0.07	0.01	0.1	0.01	0.01	9.69	10.33	12.27	0.02	0.63
21VII-TVG22-A	Silicified sulfide rich sample		60.15	0.02	0.41	0.12	0.03	0.12	0	< 0.01	13.73	11.73	0	0.08	0.11
21VII-TVG22-7	Silicified sulfide rich sample		61.76	0.04	0.17	0.03	0.01	0.06	0	< 0.01	6.8	10.65	0	0.21	11.64
	Average of massive and chimney(4)	2.65	14.76	0.03	0.26	0.05	0.03	0.11	0.01	0.02	24.69	25.84	16.47	2.05	20.75
	Average of Total(9)	1.37	43.86	0.04	0.24	0.08	0.02	0.1	0.01	0.01	16.15	17.43	11.08	0.96	11.80
Longqi-1		2.00	2.47								45.6			2.83	3.28
Duanqiao-1		0.93	18.08			0.02					28.9			2.80	2.60
Logatchev 2		25.90	3.23			1.27					19.68			20.05	22.78
Beebe		17.10				1.72					36.1			6.90	2.70
Karei		5.28	3.2								20			22.80	6.50

Elements	Pb	Mn	Co	Ni	Cd	Mo	Ag	As	Cr	Ga	Sb	Se	Sn	Ba
Unit	μg/g	μg/g	μg/g	μg/g	μg/g	μg/g	μg/g	μg/g	μg/g	μg/g	μg/g	μg/g	μg/g	μg/g
Detection limit	0.5	5	0.1	0.2	0.02	0.05	0.01	0.2	1	0.05	0.05	0.2	0.2	0.5
34II-TVG22-1–2	84	125	76.1	8.5	21.5	49.6	13.80	25.4	2	1	2.0	2.0	1.2	0.7
34II-TVG22-7	18.9	418	4.4	6.2	5.5	5.6	2.70	3.4	3	0.5	0.3	0.6	0.4	0.6
34II-TVG22-5	141	105	26.3	7.6	23.4	7.1	32.00	23.3	2	0.3	2.6	1.9	0.2	1.8
34II-TVG22-2	90	90	126.0	3	547.0	13.1	95.20	47	10	51	16.1	13.4	137.0	0.5
34II-TVG22-1	43	75	18.3	8.9	16.4	9.8	29.40	26.6	4	1.1	2.5	0.9	3.4	0.9
34II-TVG22-3	54	41	16.6	16.3	15.3	2.6	17.35	14.1	2	1	2.0	2.0	1.8	1.4
34II-TVG22-4	57	92	30.0	10.4	22.0	7.2	16.55	39.5	3	0.7	2.5	1.9	1.2	1.0
34II-TVG22-6	55	42	42.2	12.7	56.3	14.0	29.90	17	4	2.9	1.7	1.9	8.8	1.1
39II-TVG04-2	4.9	309	13.6	6.6	0.4	35.5	5.84	17.9	2	1.5	1.8	12.0	1.0	20.0
	83.5	185	58.2	6.3	149.4	18.8	35.90	24.8	4.3	13.2	5.3	4.5	34.7	0.9
	60.8	144	39.3	8.9	78.6	16.0	27.00	23.8	3.6	6.7	3.5	4.1	17.2	3.1

(*continued on next page*)

Table 2 (*continued*)

Elements	Pb	Mn	Co	Ni	Cd	Mo	Ag	As	Cr	Ga	Sb	Se	Sn	Ba
34II-TVG23-1H	76	170	64.4	6.5	15.8	17.4	97.30	15.7	1	0.4	1.5	3.4	1.1	2.0
21VII-TVG22-1	43	17	1290.0	1.3	104.0	6.1	56.30	2.3	1	15.8	1.6	8.5	66.2	2.2
21VII-TVG22-2	71	70	370.0	4	482.0	16.7	115.50	30	1	76	11.5	7.6	205.0	1.7
21VII-TVG22-A-3	29	69	994.0	1.4	609.0	13.8	36.00	275	< 1	69.3	14.7	25.0	148.0	8.7
34II-TVG23-1	67	172	21.6	5.8	5.5	11.5	54.90	14.4	1	0.1	0.4	0.3	0.2	1.0
34II-TVG23-3	144	50	72.0	4	98.8	17.7	98.20	42	1	4.2	7.0	2.6	20.0	0.5
34II-TVG23-4	64	220	26.3	5.3	10.2	14.2	43.80	13.3	2	0.2	0.4	0.4	0.2	1.1
21VII-TVG22-A	49	126	187.0	6.3	26.5	9.6	2.76	4.6	5	1.3	0.5	1.0	0.4	6.4
21VII-TVG22-7	127	93	299.4	3.9	109.0	13.4	46.74	45.9	3	10.6	8.2	5.7	27.6	9.7
	55	82	679.6	3.3	302.7	13.5	76.28	80.8	1	40.4	7.3	11.1	105.1	3.7
	75	110	369.4	4.3	162.3	13.4	61.28	49.3	2	19.8	5.1	6.1	52.1	3.7
Longqi-1	119		222.0	2.4	111.2	26.0	70.20		6		3.7			
Duanqiao-1	0.1	274	164.4	8.5	129.7	89.7	83.50	494.8			25.4	11.7	3.3	157.8
Logatchev 2	435	508	49.0	31	356.0	49.0	79.00	289		32	74.0	1314	1107	0.1
Beebe	281		237.9	7.1	88.5	45.4	114.00		3	22.6	16.2	103.6	77.4	
Karei	328		401.0	8.8	127.6	16.2	67.30	106.7			9.2	150.0	39.7	12.1

Fig. 3d).

5.2.2. Sulfide rich samples in the NES

The $\delta^{34}S$ values of 16 microdrilling samples from the two sulfide rich samples range from 3.75‰ to 8.73‰ with a median of 4.74‰ (Table 3), which is significantly higher than the SWS sulfide rich samples (Fig. 6). The pyritic massive sulfide samples (21VII-TVG22-1) show similar $\delta^{34}S$ values to that of the silicified sulfide rich chimney ones (34II-TVG23-1). At the hand specimen scale, samples composed primarily of pyrite show higher $\delta^{34}S$ values than sphalerite, and samples close to the conduit have lower $\delta^{34}S$ values.

6. Discussion

6.1. Origin of chemical elements on sulfide-rich samples

Bulk geochemistry and mineral assemblage features show that the Yuhuang-1 HF exhibits obvious mafic related HF signals. (1) Sulfide rich samples in the SWS and NES are rich in SiO_2, ranging from 10.25 to 74.86 wt% (average 43.85 wt%, N = 9) and from 5.44 to 75.70 wt% (average 43.86 wt%, N = 9), respectively. Previous studies revealed that SiO_2 concentrations in ultramafic-related HFs are relatively low (Fouquet et al., 2010). The average SiO_2 value of massive sulfide rich samples in the study area are significantly higher than those in ultramafic related HFs on Mid-Atlantic Ridge (eg. Rainbow and Logatchev with less than 1 and 6 wt% SiO_2, respectively; Fig. 7a; Fouquet et al., 2010). (2) Sulfide rich samples in ultramafic-related hydrothermal systems are characterized by higher Cu, and Au contents (> 10 wt% average Cu and > 3 ppm average Au) than mafic-related hydrothermal systems (German et al., 2016). The average Cu + Zn contents in the massive sulfide and chimney samples of SWS and NES are significantly lower than those of ultramafic-related HFs (Fig. 7a and b; Fouquet et al., 2010). Au contents of massive sulfide and chimney samples in the SWS and NES range between 0.09 and 9.09 ppm (average 2.87 ppm, N = 4) and between 0.24 and 4.73 ppm (average 2.65 ppm, N = 3), respectively, which are comparable to those of mafic-related Duanqiao-1 (0.36–1.27 ppm Au; unpublished data), Longqi-1 (2.0 ppm on average; Tao et al., 2011) on the SWIR, and Jan Mayen (1.42 and 0.71 ppm in Soria Moria and Troll Wall, respectively; Cruz, 2016), Loki's Castle (0.30 ppm on average; Cruz, 2016) on the AMOR, but significantly lower than that of Beebe (17.10 ppm on average; Webber et al., 2015) and ultramafic-related hydrothermal field on the MAR (Fig. 7c; Fouquet et al., 2010, and references therein). (3) The Ni and Co contents in the SWS and NES massive sulfide samples (Average of 6.3 ppm, 58.2 ppm in the SWS and 3.3 ppm, 679.6 ppm in the NES, respectively) are comparable to MORB-related HFs (Fig. 7d), but significantly lower than that of ultramafic-hosted massive sulfides (100–7000 ppm; Melekestseva et al., 2014, and references therein). Melekestseva et al. (2013) concluded that the Ni/Co ratios of < 1 of shallow massive and semi-massive sulfides may indicate a dominant metal contribution from a mafic rather than an ultramafic source. All of the massive sulfide samples in the Yuhuang-1 HF are characterized by Ni/Co ratios lower than 1. (4) It has been suggested that the hydrothermal leaching of ultramafic rocks tends to set up more reducing conditions and lower sulfur activity than in mafic-hosted hydrothermal systems, which results in crystallization of pyrrhotite rather than pyrite or marcasite as a major Fe sulfide (Melekestseva et al., 2014). Thus, sulfide rich samples in the mafic related HFs are usually lack of pyrrhotite, while common in ultramafic related HFs (Fouquet et al., 2010). Therefore, it could be concluded that the Yuhuang-1 HF has geochemical signatures similar to mafic related HFs.

On the other hand, the Yuhuang-1 HF also shows ultramafic-related features. Previous studies have shown that the Sn content of the massive sulfide in mafic-related HFs is generally less than 25 ppm, whereas the ultramafic-related sulfide is rich in Sn (80–1100 ppm; Fouquet et al., 2010). At high temperatures (> 300 °C), sulfides can incorporate

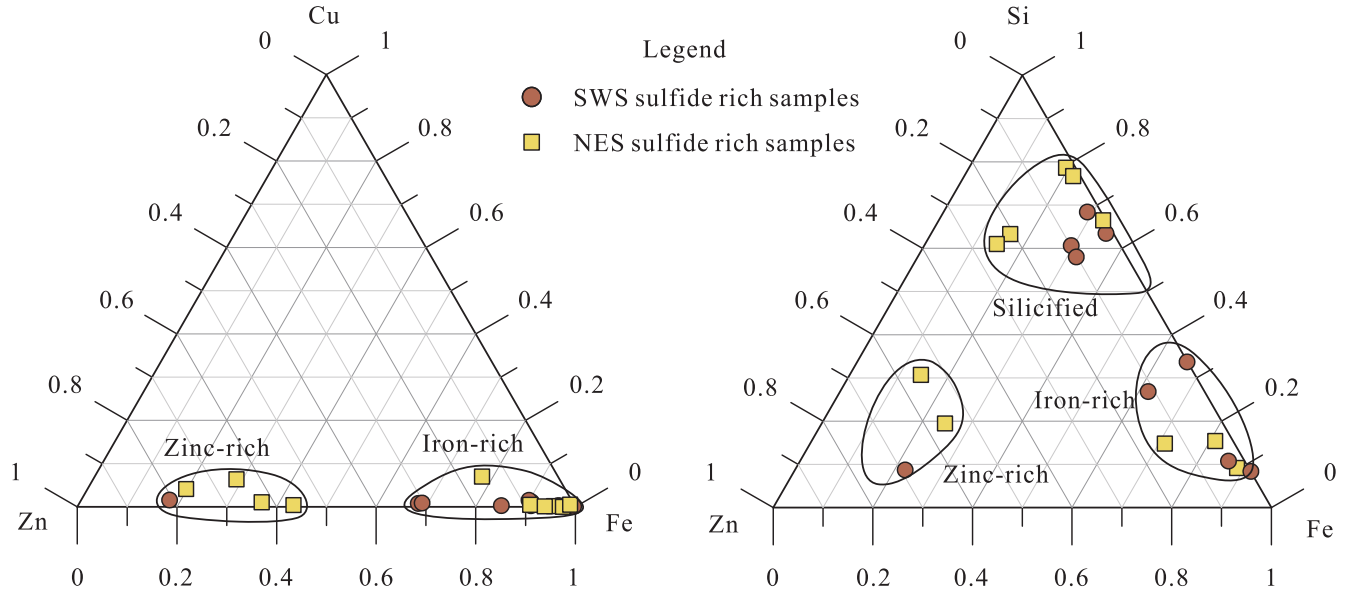

Fig. 5. Cu–Fe–Zn and Fe–Zn–Si classifications of the surface sulfides in the Yuhuang-1 HF.

Sn, and it is likely that Sn^{2+} substitutes for Fe^{2+} in high-temperature chalcopyrite (Maslennikov et al., 2009). The average Sn contents of massive sulfide samples in the SWS and NES are 34.7 and 105.1 ppm, respectively, which are comparable to the ultramafic-related HF on the MAR (Fig. 8a). In particular, the Sn contents of the sphalerite-rich massive samples of the SWS (137 ppm) and NES (205 and 148 ppm) are significantly higher than those of mafic-related HFs. In addition, Fouquet et al. (2010) concluded that massive sulfide in ultramafic-related HFs usually show low Cd/Zn ratios. Most of the massive sulfide in the Yuhuang-1 HF have similar Cd/Zn ratios to those of the ultramafic-related Logatchev and Rainbow HFs but are significantly lower than those of the mafic-related Lucky Strike and Snake Pit HFs (Fig. 8b), suggesting that they also contain ultramafic-related signals.

6.2. Sulfur isotope systematics

Previous studies have shown that the $\delta^{34}S$ values of modern MOR seafloor sulfides are characterized by minor positive values of > 0‰ (Shanks, 2001; Zeng et al., 2001, 2017; Jiang et al., 2006). In this study, the $\delta^{34}S$ values of the sulfide rich samples in the Yuhuang-1 HF are variable, ranging from −1.37‰ to 8.73‰ (Table 3). Sulfur isotope studies of the TAG HF revealed that the range of the $\delta^{34}S$ values (4.4‰–8.9‰) is much larger than that of at 21° N and 13° N on the EPR (Herzig et al., 1998b). This has been interpreted as the result of multiple mineralization processes, and the same may apply to the Yuhuang-1 HF. Sulfide rich samples in the SWS and NES show different sulfur isotopic signatures. The $\delta^{34}S$ values in the NES (median 4.74‰) are much higher than those in the SWS (median 0.83‰), whereas the pyrite vein in the silicified sample (4.09‰–6.02‰) in the SWS shows similar $\delta^{34}S$ values to the sulfide in the NES (3.75‰–8.73‰), suggesting that there probably exist two mineralization stages. In the SWS, the $\delta^{34}S$ values of pyritic massive sulfide (from −1.37‰ to 1.25‰) and silicified sample (from −0.89‰ to 2.90‰) are similar but lower than those of sphalerite-rich massive sulfide (from 0.47‰ to 2.55‰) and sulfide-vein-bearing altered basalt (from 0.43‰ to 2.27‰), indicating that the $\delta^{34}S$ of the ore-forming fluid decreased during migration from depth but was basically stable when forming the low-temperature sulfides (Fig. 9). In the NES, the silicified sulfide rich chimney shows similar $\delta^{34}S$ values to the pyritic massive sulfide. In general, the content of seawater increases during the sulfide mineralization process, leading to higher $\delta^{34}S$ in the late-stage-forming sulfide (Bluth and Ohmoto, 1988). The stable $\delta^{34}S$ of the late-stage samples in the Yuhuang-1 HF suggests that these sulfide rich samples were formed under a relatively closed condition, which is supported by the porous features and non-development of chimney and zonation structures in the samples.

Broadly, the $\delta^{34}S$ values in the SWS increase continuously from the inner part to the outer part. Fig. 3b shows that the $\delta^{34}S$ values of the rim pyrite samples are higher than those of the inner porous and conduit sphalerite samples in the sphalerite-rich massive sulfide and that the samples from the inner regions and the conduit of the pyritic massive sulfide have lower values than those of the outer region samples (Fig. 3c), suggesting that the $\delta^{34}S$ values decreased from early to late mineralization. However, the NES sulfide rich samples have inconsistent sulfur isotope distributions. Pyritic massive sulfide in the NES shows $\delta^{34}S$ values that also decrease from the inner to outer regions (Fig. 3g), with the $\delta^{34}S$ values of the inner high-temperature chalcopyrite zone being higher than those of the outer sphalerite and pyrite zone samples. Meanwhile, in the silicified sulfide rich chimney, the inner region conduit late-stage sphalerite samples have lower $\delta^{34}S$ values than the pyrite and sphalerite samples (Fig. 3h), suggesting that the $\delta^{34}S$ values can either decrease or increase during mineralization. These variations in the sulfur isotopic compositions of the hydrothermal sulfides probably resulted from different portion mixtures of the end-members controlled by variations in the permeability of the sulfide structures, the metasomatism of early sulfate minerals, the sulfur isotopic composition changes of H_2S via deep water–rock reactions during the hydrothermal system evolution, or the local disequilibrium of sulfur isotopic fractionation during sulfide deposition (Fouquet et al., 1996; Herzig et al., 1998a).

6.3. The origin and evolution of sulfur isotopes

Sulfide rich veins in the altered basalt in the SWS have a small range of $\delta^{34}S$ values (0.43‰–2.27‰), which are similar to that of H_2S in the reaction zone released to the hydrothermal system (1.0‰–1.5‰; Shanks and Seyfried, 1987; Woodruff and Shanks, 1988). Therefore, the $\delta^{34}S$ values of sulfide rich veins in altered basalt could be considered to be those of the deeper part of the hydrothermal system. In general, sulfur in the seafloor sulfide can be attributed to the mixture of MORB-derived S ($\delta^{34}S = 0.1 \pm 0.5$‰; Sakai et al., 1984) and seawater sulfate ($\delta^{34}S = 20.9$‰; Rees et al., 1978), showing slight enrichment in $\delta^{34}S$ relative to magmatic sulfur (Davis et al., 2003). The $\delta^{34}S$ values of the sulfide rich samples in the SWS of the Yuhuang-1 HF are characterized by negative $\delta^{34}S$ (down to −1.37‰), which are currently the lowest

Table 3
Sulfur isotope composition of the sulfide rich samples in the Yuhuang-1 HF.

Area	Sample	Sulfide type	Serial Number	Mineral composition	$\delta^{34}S$(‰)
SWS	39II-TVG04	Sulfide vein bearing altered basalt	1	whole rock	2.27
			2	altered basalt	0.43
			3	whole rock	0.95
	34II-TVG22-2	Sphalerite-rich massive sulfide	1	Sph + Py	2.55
			2	Sph	0.75
			3	Sph	0.49
			4	Sph	0.8
			5	Sph	0.53
			6	Sph	0.47
	34II-TVG22-7	Pyritic massive sulfide	1	Py	−1.37
			2	Py	−0.47
			3	Py + Si	0.11
			4	Si + Py	0.13
			5	Si + Py	0.58
			6	Si + Py	1.18
			7	Py	−1.09
			8	Si + Py	1.25
	34II-TVG22-1	Silicified sulfide rich sample	1	Sph + Si	−0.89
			3	Sph	2.9
			5	Sph	2.08
			6	Sph + Py	1.87
			7	Sph	−0.97
			9	Sph	2.75
			11	Si + Sph	1.34
			14	Sph + Py	1.01
		Pyrite vein	2	Si + Py	5.91
			4	Sph + Py	4.56
			8	Py + Sph	5.72
			10	Py + Sph	4.09
			12	Py + Sph	5.98
			13	Py + Sph	6.02
	34II-TVG22-4	Silicified sulfide rich sample	1	Si + Py	1.04
			2	Py	2.65
			3	Si + Py	0.83
			4	Py + Si	0.69
			5	Py + Sph	−0.34
			6	Si + Py	0.07
	34II-TVG22-5	Silicified sulfide rich sample	1	Py	1.32
			2	Si + Py	−0.68
			3	Si + Py	−0.02
			4	Sph + Si	−0.76
NES	21VII-TVG22-1	Pyritic massive sulfide	1	Py	4.61
			2	Py + Sph	4.13
			3	Py + Sph	4.15
			4	Sph + Py	3.99
			5	Ccp + Sph + Py	5.77
			6	Sph + Ccp + Py	8.73
	34II-TVG23-1	Silicified sulfide rich chimney	1	Sph	3.75
			2	Sph	4.46
			3	Py + Sph	7.47
			4	Sph	4.52
			5	Sph	5.6
			6	Sph	5.45
			7	Sph + py	7.25
			8	Sph + py	4.14
			9	Sph	7.07
			10	Sph	7.11

The serial numbers represent the microdrilling samples, and their locations are shown in Fig. 3. Mineral abbreviations are the same as in Fig. 4.

values obtained on ultraslow-spreading ridges (Fig. 10). Therefore, these sulfur isotope signatures cannot be simply explained by the mixing of seawater and basaltic-derived hydrothermal fluid. Currently, there are several explanations for the negative sulfur isotopic composition, as listed below.

(1) The negative $\delta^{34}S$ features may be caused by disproportionation of SO_2 into H_2S and H_2SO_4 during magmatic degassing, accompanied by kinetic isotope fractionation which causing deposited sulfide and sulfate minerals exhibit $\delta^{34}S$ values lighter and heavier than magmatic SO_2, respectively (Ohmoto, 1979). Magmatic degassing has been attributed to the main factor that causing negative $\delta^{34}S$ features of the sulfide in the Hine Hina Vent Field in the Lau back-arc (Herzig et al., 1998a), the Conical Seamount (Petersen et al., 2002), and the Snowcap Vent Site (Roberts et al., 2003), Susu knolls and PACMANUS (Kim et al., 2004) in the Manus Basin. However, sulfide rich veins in the altered basalt, which probably represents the high temperature hydrothermal products, show positive $\delta^{34}S$ values that are higher than those of surface sulfide rich samples in the SWS. If these sulfide veins formed by magmatic degassing fluid, they should exhibit lower $\delta^{34}S$ values than surface sulfide rich samples. Thus, negative $\delta^{34}S$ values caused by magma degassing can be excluded.

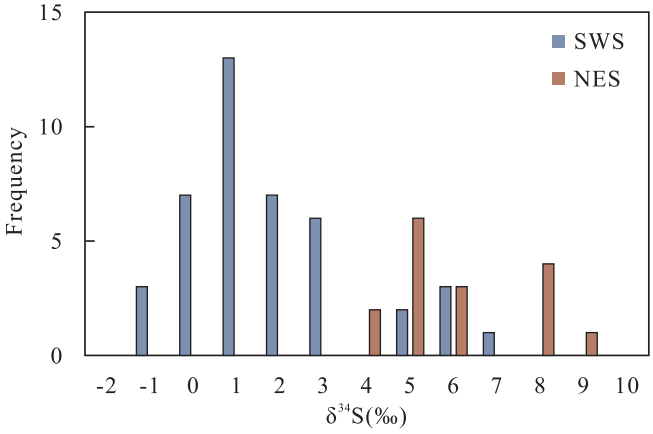

Fig. 6. Sulfur isotope composition histogram of the Yuhuang-1 HF.

(2) SO_2 degassing of the basalt could lead to a negative sulfur isotopic composition of the basalt (Alt et al., 1989); therefore, sulfur leached from SO_2 degassed basalt likely has negative $\delta^{34}S$ values. High temperature sulfide with negative $\delta^{34}S$ values, of which range from –2.17 to –0.3‰ in hydrothermal system on Loihi Seamount (Davis et al., 2003), and a lowest value of −3.26‰ were observed at Semenov-1 (Melekestseva et al., 2014). However, basalt in the study area shows no apparent porous features that caused by gas degassing. In addition, sulfide rich veins in the altered basalt exhibit higher $\delta^{34}S$ values than those of surface sulfide rich samples, indicating a decrease of $\delta^{34}S$ values during mineralization. Thus, negative $\delta^{34}S$ values caused by leaching from SO_2-degassed basalt can be excluded also.

(3) Volatiles of H_2S and H_2 degassing during phase separation of the fluid could result in an increase in the redox state of the liquid phase, leading to an increase and/or decrease of the sulfur isotopic composition of the fluid and volatile phases, respectively (Mckibben and Eldridge, 1990; Rouxel et al., 2004). As a result, sulfide formed via the volatile phase is generally rich in light S isotopes. However, the Yuhuang-1 HF is located at a water depth of approximately 1400 m, and phase separation must have occurred in the deep part. Consequently, sulfide rich samples formed from the condensed volatile phase in the SWS and NES would have relatively uniform sulfur isotope compositions. Therefore, this mechanism cannot explain the negative sulfur isotope feature.

(4) Bacterial activity may also be responsible for the negative $\delta^{34}S$ values. On sediment-covered ridges such as the Guaymas Basin, negative sulfur isotope sulfide values are commonly observed (Peter and Shanks, 1992). Bacteriogenic sulfur in the vent fluids produces sulfides with $\delta^{34}S$ values as low as −3.7‰ (Herzig et al., 1998a). On sediment-starved ridges, it has been reported that sub-seafloor bacterial reduction of seawater sulfate generated light sulfur isotope (−0.5‰) of the low-temperature sulfide at Lucky Strike (Rouxel et al., 2004). The Yuhuang-1 HF is located on the south

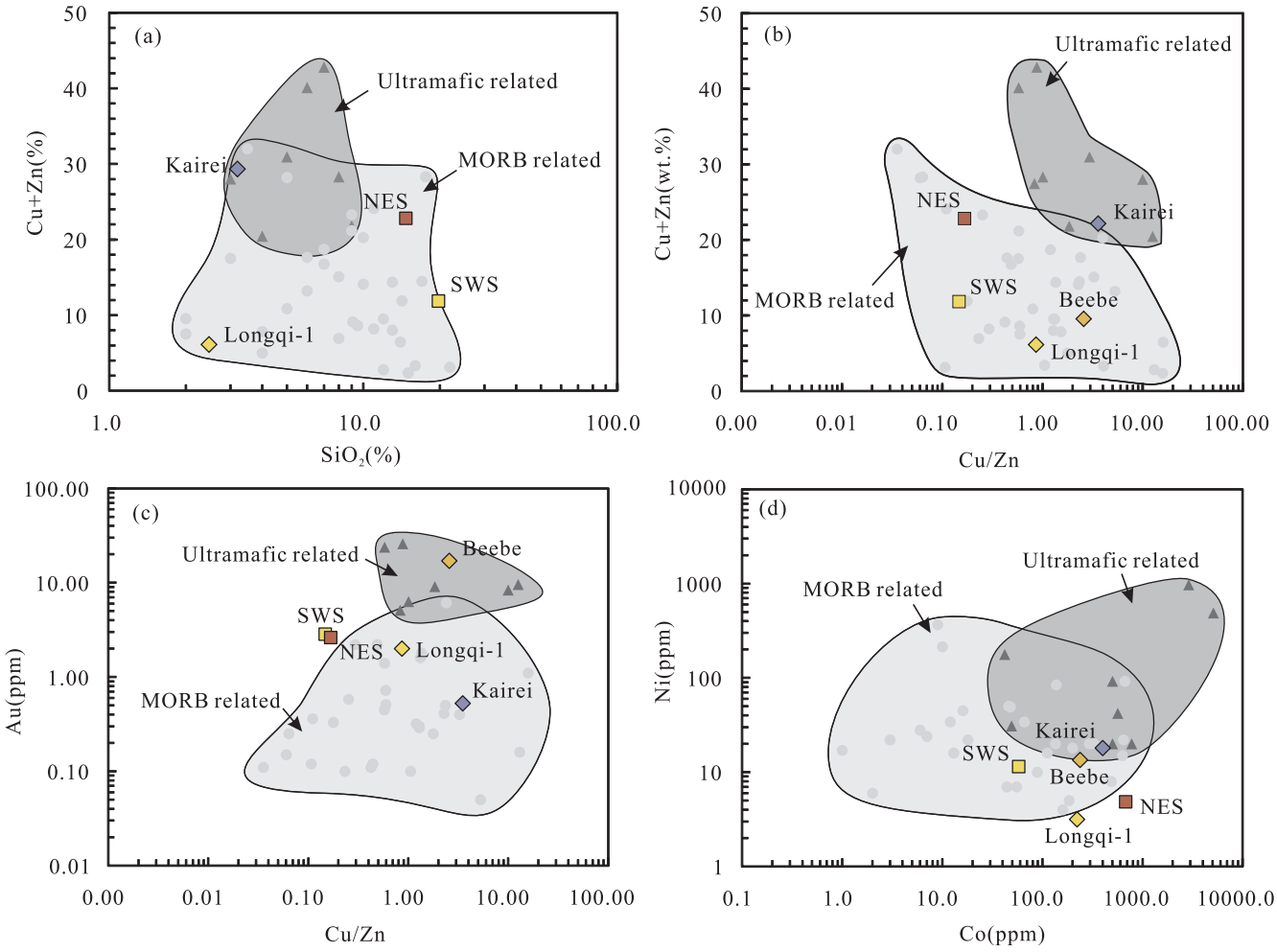

Fig. 7. (a) SiO_2 versus Cu + Zn, (b) Cu/Zn versus Cu + Zn, (c) Cu/Zn versus Au and (d) Co versus Ni diagrams of the Yuhuang-1 HF. The data of the mafic- and ultramafic-related HFs on the MAR are from Fouquet et al. (2010) and references therein; the data of the HFs of Juan de Fuca, Explorer, and EPR are from Hannington et al. (2005) and references therein; Kairei: Wang et al. (2014); Beebe: Webber et al. (2015); and Longqi-1: Tao et al. (2011).

wall of the rift valley with a height of more than 1500 m, with sediments poorly developed. Therefore, sediment-derived bacterial sulfur may not be appropriate. However, previous studies have shown that microbial activity is abundant in oceanic serpentinization environments (Szynkiewicz et al., 2009; Schwarzenbach et al., 2016) and produces an increase in sulfide–sulfur contents with low $\delta^{34}S$ sulfide values for an open system and high $\delta^{34}S$ sulfide values for a closed system, which has been observed at the Iberian margin and Lost city(Alt et al., 2007; Delacour et al., 2008), and even in altered oceanic basalts at ODP Site 801(Rouxel et al., 2008). Sulfur derived from the same origin would generate sulfide with negative $\delta^{34}S$ features. In the Yuhuang-1 HF, (a) the serpentine sampled with the TV-grab suggests that there are likely ultramafic outcrops; (b) silicified sulfide rich samples, which is usually thought to be related

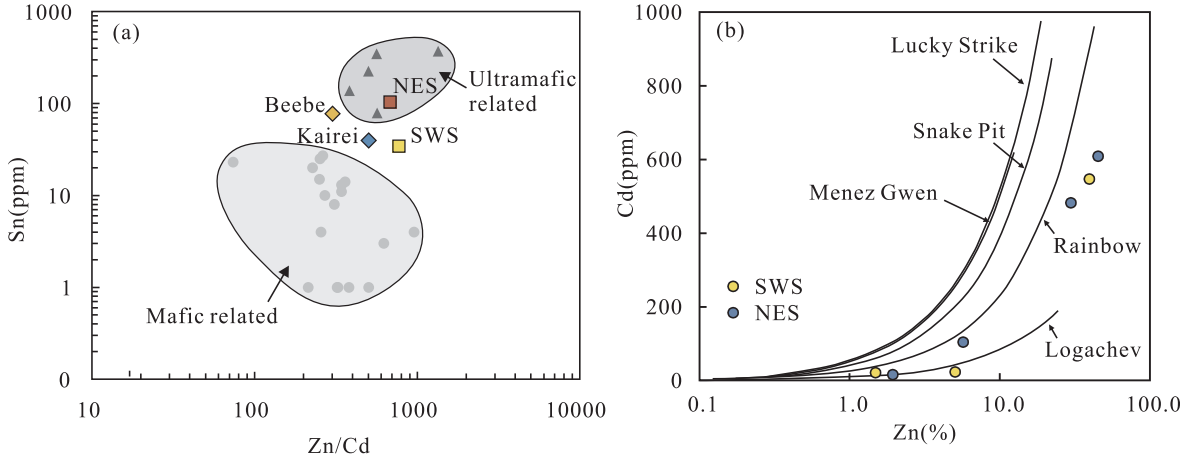

Fig. 8. (a) Zn/Cd vs Sn and (b) Zn vs Cd diagram (following Fouquet et al., 2010) of the Yuhuang-1 HF. Data base are the same with Fig. 7.

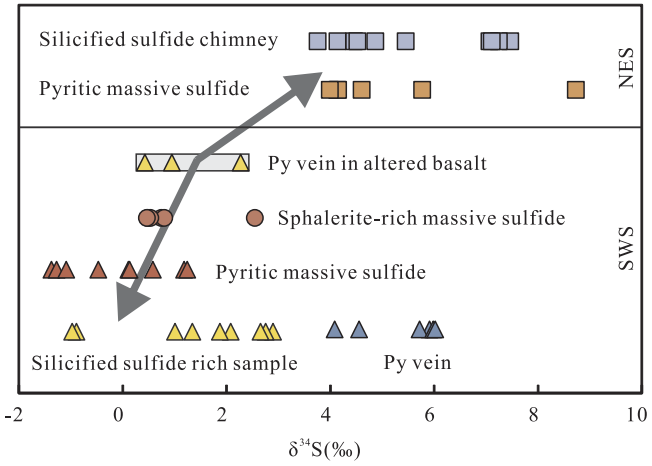

Fig. 9. Sulfur isotope distribution range of different mineralization of the Yuhuang-1 HF.

to the bacterial activities (Dekov et al., 2015), is developed in this area; and (c) pyrite with biogenic relics structures were identified under microscope. Therefore, we suggest that bacteria-derived sulfur could cause the negative $\delta^{34}S$ signatures in the SWS sulfide rich samples.

Seafloor sulfide rich samples in the NES shows $\delta^{34}S$ values ranging from 3.75‰ to 8.73‰. Previous studies show that $\delta^{34}S$ values in excess of 4.5‰ can only be explained by the reaction of seawater within the feeder zones immediately underlying the seafloor deposits (Janecky and Shanks, 1988). Additional SO_4 may be reduced via reactions with Fe-bearing silicates (Alt et al., 1989), resulting in aqueous $\delta^{34}S_{H2S}$ values that are commonly as high as approximately 6‰–7‰ (Shanks, 2001). This result suggests that the formation of sulfide rich samples in the NES includes deep seawater circulation processes.

6.4. Contribution of bacteria-derived sulfur

The formation of sulfide rich samples in the SWS includes the participation of crustal rocks, seawater, and biologically derived sulfur, where sulfide rich samples in the NES are primarily formed by the mixing of seawater and crustal rocks derived sulfur and have experienced sub-seafloor seawater reduction. Due to similar geological background and geochemical composition features of sulfides from the SWS and NES, it is reasonable to assume that the average $\delta^{34}S$ value of sulfide rich samples in the SWS and NES would be close to each other, if the ore-forming fluid of the SWS without biological sulfur input. Then, we could provide a semi-quantitative model to evaluate S that derived from microbial activity from the SWS. Based upon S mass balance

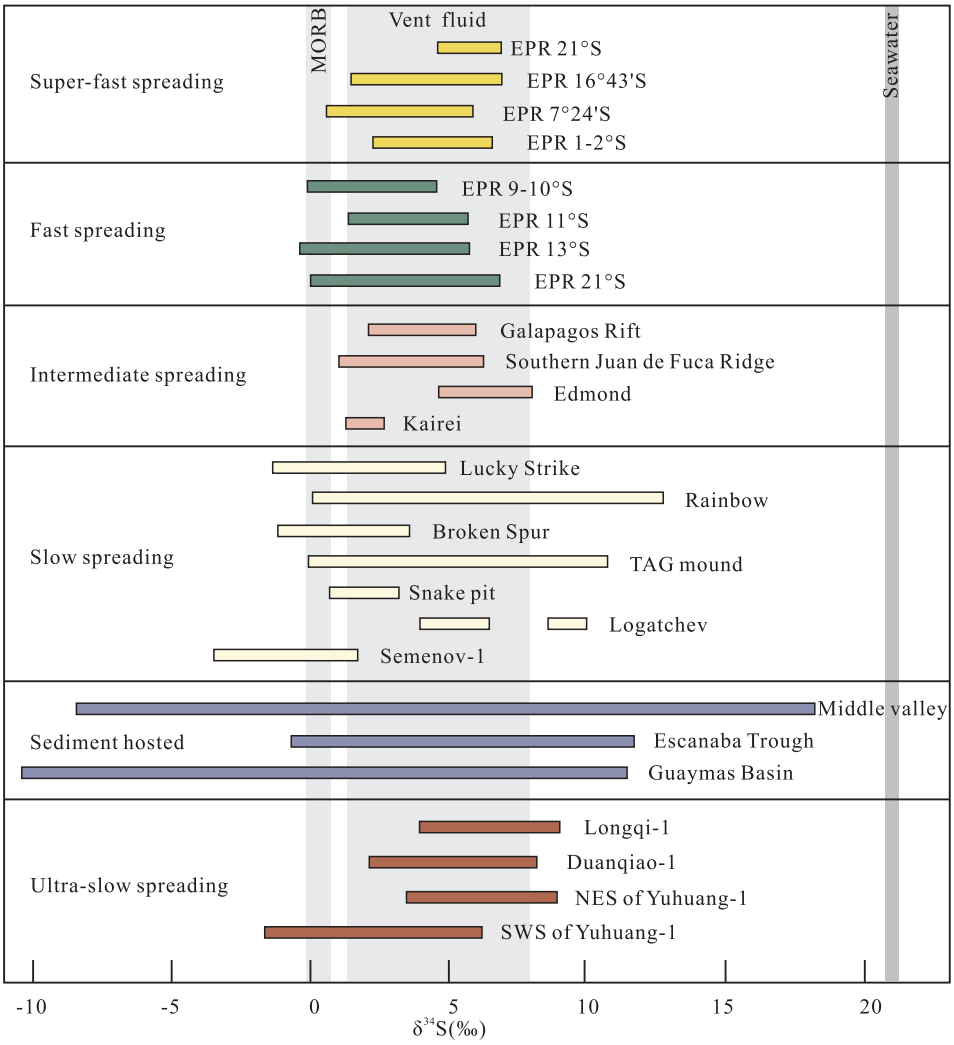

Fig. 10. Sulfur isotope comparison of Yuhuang-1 to other HFs. Data are from Zeng et al. (2017) and references therein; Semenov-1: Melekestseva et al. (2014); Duanqiao-1: Yang et al. (2017); Longqi-1: Ye et al. (2012) and Zeng et al. (2017).

model, the biological sulfur input ratio of the SWS sulfide rich samples can be roughly calculated using the following formula that suggested by Zeng et al., (2017):

$$\delta^{34}S_{mix} = X\times \delta^{34}S_{Biogenic} + (1-X) \times \delta^{34}S_{Hydrothermal},$$

where X is the amount of the biogenic component ($\delta^{34}S_{Biogenic}$) and $\delta^{34}S_{Hydrothermal}$ is the sulfur isotopic composition of the hydrothermal fluid. Although a mixture between the S derived from crustal (or mantle) rocks and S derived from seawater has varied $\delta^{34}S$ values, most of HFs on mid ocean ridges, without microbial activity, have $\delta^{34}S$ values ranging from 1 to 9‰, with an average value of 4.7‰ (Zeng et al., 2017), similar to the median $\delta^{34}S$ value of the NES silicified sulfide rich chimneys (4.74‰). Thus, we conclude that this value of 4.74‰ could be used as an end-member of S that mixed from seawater and crustal rocks. Previous studies have shown that biological sulfur usually has a $\delta^{34}S$ value ranging from −40‰ to −10‰ (Brunner and Bernasconi, 2005; Delacour et al., 2008). Therefore, it can be calculated that, in order to form silicified sulfide rich samples with an average $\delta^{34}S$ value of 0.82‰ in the SWS, the proportion of biologically derived sulfur is likely approximately 10%–25%, which is lower than that in HFs on sediment-covered ridges (Peter and Shanks, 1992; Stuart et al., 1994).

6.5. Possible ore-forming process

The topography of the segment where the Yuhuang-1 HF located is characterized by RVA and non-transform discontinuities. Deep tow observation and TV grab sampling suggested that basalts are developed in most of the area. Therefore, the outcrops of the ultramafic rocks revealed by TV grab sampling are likely exposed by a detachment fault (Zhou and Dick, 2013). However, the topography where these ultramafic rocks sampled lacks typical oceanic core complex features, implying that the detachment fault is likely to be newly developed (Zhou and Dick, 2013), which may be the reason for the bulk geochemistry signals that show both mafic and ultramafic related HF features. Currently, the involvement of multiple origins of ore forming elements has been proposed to explain the geochemical features of several HFs, including Rainbow (Marques et al., 2006, 2007), Logatchev (Augustin et al., 2008), Kairei (Nakamura et al., 2008) and Semenov-2 (Melekestseva et al., 2017), among others. Similar to ore-forming processes in other HFs, the infiltrating seawater was heated by deep magma and has leached metal elements from basement rocks generating an ore-forming fluid (Tivey, 2007). This ore-forming fluid is characterized by $\delta^{34}S$ values of approximately 1.5‰. Accompanied by fluid migration along the faults and cracks, sulfide rich ore veinlets with nearly unchanged $\delta^{34}S$ values formed.

The SWS and NES are located at a distance of about 500 m from each other. However, sulfide rich samples in the SWS and NES show distinct differences on sulfur isotopes features, and also exhibit differences on mineral assemblages. Therefore, we favor that they probably formed at different stages. During sulfide formation in the SWS, a possibly bacteria-derived fluid, which may consist of 10%–25% of the total sulfur component, was mixed with the ore-forming fluid, resulting in negative $\delta^{34}S$ values. At this stage, a modest amount of seawater was added to the fluid. During the formation of the NES sulfide rich samples, the seawater component increased, and a possible seawater–hydrothermal fluid sub-seafloor reaction zone developed. The occurrence of abundant amorphous silicon and the wide range of $\delta^{34}S$ values in the sulfide rich samples also suggest that the SWS and NES were relatively mature and affected by late-stage hydrothermal modifications, similarly to the sulfate-sulfide chimneys from Kuroko area, Mariana Trough (Shikazono and Kusakabe, 1999).

7. Conclusions

(1) The surface sulfide rich samples in the SWS and NES of the Yuhuang-1 HF are mainly composed of pyrite, sphalerite, marcasite, chalcopyrite, and amorphous silicon with additionally pyrrhotite in the NES. The contents of silicon in the sulfide rich samples are extremely high with an average of about 45%. On the basis of the primary mineral assemblages and mineralization elements, the surface sulfide rich samples can be divided into zinc-rich, iron-rich, and silicified samples.

(2) Sulfide rich samples in the SWS and NES have similar elemental abundances. Au, Co, Ni, and Si contents and Ni/Co ratio features of the samples are similar to those of a mafic-related hydrothermal field, and the Sn content and the Cd/Zn ratio are comparable to ultramafic-related hydrothermal fields. The dominant basaltic host rock coexisting with newly developed detachment faults are probably responsible for these features.

(3) Surface sulfide rich samples in the Yuhuang-1 HF exhibit a large range of $\delta^{34}S$ values, with the lowest $\delta^{34}S$ value (−1.37‰) currently observed in HFs on ultraslow-spreading ridges. The negative $\delta^{34}S$ values in the SWS were likely caused by a mixture with bacteria-derived sulfur, which may be responsible for 10%–25% of the total sulfur component. Sulfide rich samples in the NES show obviously higher sulfur isotope compositions (3.75‰–8.73‰ with a median of 4.74‰) than those in the SWS owing to sub-seafloor seawater reduction. Sulfide rich samples in the SWS and NES were likely produced in different stages of hydrothermal activity.

Acknowledgments

This research was funded by China Ocean Mineral Resources R & D Association (COMRA) Project (DY135-S1-1-01, 02), the National Key Research and Development Program of China (2017YFC0306800, 2017YFC0306603 and 2016YFC0304905), Central Public-Interest Scientific Institution Basal Research Fund (JG1606), and the International seabed authority Endowment Fund: International cooperative study of seafloor massive sulfides exploration and environmental evaluation at slow and ultra-slow spreading ridges. We are grateful to the captains and crews of the DY115-21, DY125-34 and DY125-39 cruises on R/V DayangYihao, who contributed to the success of this project. We are also grateful for the constructive comments and suggestions from Chief Editor Franco Pirajno, Professor Georgy Cherkashov and two another anonymous reviewers.

References

Alt, J.C., Anderson, T.F., Bonnell, L., 1989. The geochemistry of sulfur in a 1.3 km section of hydrothermally altered oceanic crust, DSDP Hole 504B. Geochim. Cosmochim. Acta 53 (5), 1011–1023.

Alt, J.C., Shanks III, W.C., Bach, W., Paulick, H., Garrido, C.J., Beaudoin, G., 2007. Hydrothermal alteration and microbial sulfate reduction in peridotite and gabbro exposed by detachment faulting at the Mid-Atlantic Ridge, 15°20′N (ODP Leg 209): a sulfur and oxygen isotope study. Geochem. Geophys. Geosyst. 8 (8), 13–23.

Augustin, N., Lackschewitz, K.S., Kuhn, T., Devey, C.W., 2008. Mineralogical and chemical mass changes in mafic and ultramafic rocks from the Logatchev hydrothermal field (MAR 15°N). Mar. Geol. 256 (1–4), 18–29.

Baker, E.T., Edmonds, H.N., Michael, P.J., Bach, W., Dick, H., Snow, J.E., Walker, S.L., Banerjee, N.R., Langmuir, C.H., 2004. Hydrothermal venting in magma deserts: The ultraslow-spreading Gakkel and Southwest Indian Ridges. Geochem. Geophys. Geosyst. 5 (8), Q08002.

Baumberger, T., Früh-Green, G.L., Thorseth, I.H., Lilley, M.D., Hamelin, C., Bernasconi, S.M., Okland, I.E., Pedersen, R.B., 2016. Fluid composition of the sediment-influenced Loki's Castle vent field at the ultra-slow spreading Arctic Mid-Ocean Ridge. Geochim. Cosmochim. Acta 187, 156–178.

Beaulieu, S.E., Baker, E.T., German, C.R., 2015. Where are the undiscovered hydrothermal vents on oceanic spreading ridges? Deep-Sea Res. PT II 121 (SI), 202–212.

Bluth, G.J., Ohmoto, H., 1988. Sulfide-sulfate chimneys on the East Pacific Rise, 11° and 13°N latitudes. Part II: sulfur isotopes. Can. Mineral. 26 (3), 487–504.

Brunner, B., Bernasconi, S.M., 2005. A revised isotope fractionation model for dissimilatory sulfate reduction in sulfate reducing bacteria. Geochim. Cosmochim. Acta 69 (20), 4759–4771.

Cannat, M., Rommevaux-Jestin, C., Sauter, D., Deplus, C., Mendel, V., 1999. Formation of the axial relief at the very slow spreading Southwest Indian Ridge (49° to 69°E). J. Geophys. Res. Atmos. 104 (B10), 22825–22843.

Connelly, D.P., Copley, J.T., Murton, B.J., Stansfield, K., Tyler, P.A., German, C.R., Van

Dover, C.L., Amon, D., Furlong, M., Grindlay, N., 2012. Hydrothermal vent fields and chemosynthetic biota on the world's deepest seafloor spreading centre. Nat. Commun. 3, 620–628.
Cruz, M.I.F.S., 2016. Mineralogy and Geochemistry of Contrasting Hydrothermal Systems on the Arctic Mid Ocean Ridge (AMOR): The Jan Mayen and Loki's Castle Vent Fields. University of Lisbon pp. 257.
Davis, A.S., Clague, D.A., Zierenberg, R.A., Wheat, C.G., Cousens, B.L., 2003. Sulfide formation related to changes in the hydrothermal system on Loihi Seamount, Hawai'i, following the seismic event in 1996. Can. Mineral. 41 (2), 457–472.
Dekov, V.M., Lalonde, S.V., Kamenov, G.D., Bayon, G., Shanks III, W.C., Fortin, D., Fouquet, Y., Moscati, R.J., 2015. Geochemistry and mineralogy of a silica chimney from an inactive seafloor hydrothermal field (East Pacific Rise, 18°S). Chem. Geol. 415, 126–140.
Delacour, A., Frueh-Green, G.L., Bernasconi, S.M., Kelley, D.S., 2008. Sulfur in peridotites and gabbros at Lost City (30°N, MAR): Implications for hydrothermal alteration and microbial activity during serpentinization. Geochim. Cosmochim. Acta 72 (20), 5090–5110.
Dick, H.J., Lin, J., Schouten, H., 2003. An ultraslow-spreading class of ocean ridge. Nature 426 (6965), 405–412.
Dong, S.F., Chen, D.Z., Qing, H.R., Jiang, M.S., Zhou, X.Q., 2013. In situ stable isotopic constraints on dolomitizing fluids for the hydrothermally-originated saddle dolomites at Keping, Tarim Basin. Chinese Sci. Bull. 58 (23), 2877–2882.
Edmonds, H.N., Michael, P.J., Baker, E.T., Connelly, D.P., Snow, J.E., Langmuir, C.H., Dick, H., Muhe, R., German, C.R., Graham, D.W., 2003. Discovery of abundant hydrothermal venting on the ultraslow-spreading Gakkel ridge in the Arctic. Nature 421 (6920), 252–256.
Eiler, J.M., Bergquist, B., Bourg, I., Cartigny, P., Farquhar, J., Gagnon, A., Guo, W., Halevy, I., Hofmann, A., Larson, T.E., Levin, N., Schauble, E.A., Stolper, D., 2014. Frontiers of stable isotope geoscience. Chem. Geol. 372, 119–143.
Fouquet, Y., Cambon, P., Etoubleau, J., Charlou, J.L., OndréAs, H., Barriga, F.J.A.S., Cherkashov, G., Semkova, T., Poroshina, I., Bohn, M., Donval, J.P., Henry, K., Murphy, P., Rouxel, O., 2010. Geodiversity of hydrothermal processes along the Mid-Atlantic Ridge–Ultramafic-hosted mineralization: A new type of oceanic Cu-Zn-Co-Au volcanogenic massive sulfide deposit, pp. 321–368. In: Rona, P.A., Devey, C.W., Dyment, J., Murton, B.J. (Eds.), Diversity of Hydrothermal Systems on Slow Spreading Ocean Ridges. American Geophysical Union, Washington DC, pp. 440.
Fouquet, Y., Knott, R., Cambon, P., Fallick, A., Rickard, D., Desbruyeres, D., 1996. Formation of large sulfide mineral deposits along fast spreading ridges. Example from off-axial deposits at 12°43′N on the East Pacific Rise. Earth Planet. Sci. Lett. 144 (1), 147–162.
Georgen, J.E., Lin, J., Dick, H.J.B., 2001. Evidence from gravity anomalies for interactions of the Marion and Bouvet hotspots with the Southwest Indian Ridge: Effects of transform offsets. Earth Planet. Sci. Lett. 187 (3–4), 283–300.
German, C.R., Baker, E.T., Mevel, C., Tamaki, K., 1998. Hydrothermal activity along the southwest Indian ridge. Nature 395 (6701), 490–493.
German, C.R., Bowen, A., Coleman, M.L., Honig, D.L., Huber, J.A., Jakuba, M.V., Kinsey, J.C., Kurz, M.D., Leroy, S., Mcdermott, J.M., 2010. Diverse styles of submarine venting on the ultraslow spreading Mid-Cayman Rise. Proc. Natl. Acad. Sci. 107 (32), 14020–14025.
German, C.R., Petersen, S., Hannington, M.D., 2016. Hydrothermal exploration of mid-ocean ridges: Where might the largest sulfide deposits be forming? Chem. Geol. 420, 114–126.
Han, X.Q., Wang, Y.J., Qiu, Z.Y., Liu, Y., Qiu, B.B., 2015. Discovery and mineralization features of the Yuhuang-1 hydrothermal field on Southwest Indian Ridge. Acta Miner. Sin. 35 (S1), 1141–1142 (In Chinese with English abstract).
Han, X.Q., Wu, G.H., Cui, R., Qiu, Z.Y., Deng, X.M., Wang, Y.J., 2010. Discovery of a hydrothermal sulfide deposit on the Southwest Indian Ridge at 49.2°E, American Geophysical Union, Fall Meeting, abstract #OS21C-1531.
Hannington, M.D., de Ronde, C.D., Petersen, S., 2005. Sea-floor tectonics and submarine hydrothermal systems. Econ. Geol. 100, 111–141.
Hannington, M., Jamieson, J., Monecke, T., Petersen, S., Beaulieu, S., 2011. The abundance of seafloor massive sulfide deposits. Geology 39 (12), 1155–1158.
Herzig, P.M., Hannington, M.D., Arribas Jr, A., 1998a. Sulfur isotopic composition of hydrothermal precipitates from the Lau back-arc: implications for magmatic contributions to seafloor hydrothermal systems. Miner. Deposita 33 (3), 226–237.
Herzig, P.M., Petersen, S., Hannington, M.D., 1998b. Geochemistry and sulfur-isotopic composition of the TAG hydrothermal mound, Mid-Atlantic Ridge, 26°N. Proceedings-Ocean Drilling Program Scientific Results. Natl. Sci. Found. 158, 47–70.
Janecky, D.R., Shanks III, W.C., 1988. Computational modeling of chemical and sulfur isotopic reaction processes in seafloor hydrothermal systems: chimneys, massive sulfides, and subjacent alteration zones. Can. Mineral. 26, 805–825.
Jiang, S.Y., Yang, T., Li, L., Zhao, K.D., Ling, H.F., 2006. Lead and sulfur isotopic compositions of sulfides from the TAG hydrothermal field, Mid-Atlantic Ridge. Acta Petrol. Sin. 22 (10), 2597–2602 (In Chinese with English abstract).
Kim, J., Lee, I., Lee, K.Y., 2004. S, Sr, and Pb isotopic systematics of hydrothermal chimney precipitates from the Eastern Manus Basin, western Pacific: evaluation of magmatic contribution to hydrothermal system. J. Geophys. Res. Solid Earth 109, B12210.
Kinsey, J.C., German, C.R., 2013. Sustained volcanically-hosted venting at ultraslow ridges: piccard hydrothermal field, Mid-Cayman Rise. Earth Planet. Sci. Lett. 380, 162–168.
Li, J.B., Jian, H.C., Chen, Y.S.J., Singh, S.C., Ruan, A., Qiu, X.L., Zhao, M.H., Wang, X.G., Niu, X.G., Ni, J.Y., Zhang, J.Z., 2015. Seismic observation of an extremely magmatic accretion at the ultraslow spreading Southwest Indian Ridge. Geophys. Res. Lett. 42 (8), 2656–2663.
Marques, A.F.A., Barriga, F., Chavagnac, V., Fouquet, Y., 2006. Mineralogy, geochemistry, and Nd isotope composition of the Rainbow hydrothermal field, Mid-Atlantic Ridge. Miner. Deposita 41 (1), 52–67.
Marques, A.F.A., Barriga, F.J.A.S., Scott, S.D., 2007. Sulfide mineralization in an ultramafic-rock hosted seafloor hydrothermal system: From serpentinization to the formation of Cu–Zn–(Co)-rich massive sulfides. Mar. Geol. 245 (1–4), 20–39.
Maslennikov, V.V., Maslennikova, S.P., Large, R.R., Danyushevsky, L.V., 2009. Study of trace element zonation in vent chimneys from the Silurian Yaman-Kasy volcanic-hosted massive sulfide deposit (Southern Urals, Russia) using Laser Ablation-Inductively Coupled Plasma Mass Spectrometry (LA-ICPMS). Econ. Geol. 104 (8), 1111–1141.
Mckibben, M.A., Eldridge, C.S., 1990. Radical sulfur isotope zonation of pyrite accompanying boiling and epithermal gold deposition: a SHRIMP study of the Valles Caldera, New Mexico. Econ. Geol. 85 (8), 1917–1925.
Melekestseva, I.Y., Maslennikov, V.V., Tret Yakov, G.A., Nimis, P., Beltenev, V.E., Rozhdestvenskaya, I.I., Maslennikova, S.P., Belogub, E.V., Danyushevsky, L., Large, R., 2017. Gold-and silver-rich massive sulfides from the Semenov-2 hydrothermal field, 13° 31.13′ N, Mid-Atlantic Ridge: A case of magmatic contribution? Econ. Geol. 112 (4), 741–773.
Melekestseva, I.Y., Tret'Yakov, G.A., Nimis, P., Yuminov, A.M., Maslennikov, V.V., Maslennikova, S.P., Kotlyarov, V.A., Beltenev, V.E., Danyushevsky, L.V., Large, R., 2014. Barite-rich massive sulfides from the Semenov-1 hydrothermal field (Mid-Atlantic Ridge, 13°30.87′N): Evidence for phase separation and magmatic input. Mar. Geol. 349, 37–54.
Melekestseva, I.Y., Zaykov, V.V., Nimis, P., Tret'Yakov, G.A., Tessalina, S.G., 2013. Cu–(Ni–Co–Au)-bearing massive sulfide deposits associated with mafic–ultramafic rocks of the Main Urals Fault, South Urals: geological structures, ore textural and mineralogical features, comparison with modern analogs. Ore Geol. Rev. 52 (4), 18–36.
Nakamura, K., Morishita, T., Takai, K., Hara, K., Kumagai, H., 2008. Serpentinized olivine-rich gabbros near the Kairei Hydrothermal Field Central Indian Ridge: a key to understanding the unique chemistry of the vent fluid. Geochim. Cosmochim. Acta 72 (72).
Nayak, B., Halbach, P., Pracejus, B., Münch, U., 2014. Massive sulfides of Mount Jourdanne along the super-slow spreading Southwest Indian Ridge and their genesis. Ore Geol. Rev. 63, 115–128.
Ohmoto, H., 1979. Isotopes of sulfur and carbon. In: Barnes, H.L. (Ed.), Geochemistry of Hydrothermal Ore Deposits. Wiley, New York, pp. 509–567.
Paradis, S., Jonasson, I.R., Lecheminant, G.M., Watkinson, D.H., 1988. Two zinc-rich chimneys from the plume site, southern Juan-De-Fuca ridge. Can. Mineral. 26 (3), 637–654.
Pedersen, R.B., Rapp, H.T., Thorseth, I.H., Lilley, M.D., Barriga, F., Baumberger, T., Flesland, K., Fonseca, R., Fruh-Green, G.L., Jorgensen, S.L., 2010. Discovery of a black smoker vent field and vent fauna at the Arctic Mid-Ocean Ridge. Nat. Commun. 1 (126).
Peter, J.M., Shanks Iii, W.C., 1992. Sulfur, carbon, and oxygen isotope variations in submarine hydrothermal deposits of Guaymas Basin, Gulf of California, USA. Geochim. Cosmochim. Acta 56 (56), 2025–2040.
Petersen, S., Herzig, P.M., Hannington, M.D., Jonasson, I.R., Arribas, A., 2002. Submarine gold mineralization Near Lihir Island, New Ireland Fore-Arc, Papua New Guinea. Econ. Geol. 97 (8), 1795–1813.
Rees, C.E., Jenkins, W.J., Monster, J., 1978. Sulphur isotopic composition of ocean water sulfate. Geochim. Cosmochim. Acta 42 (4), 377–381.
Roberts, S., Bach, W., Binns, R.A., Vanko, D.A., Yeats, C.J., Teagle, D.A.H., Blacklock, K., Blusztajn, J.S., Boyce, A.J., Cooper, M.J., Holland, N., Mcdonald, B., 2003. Contrasting evolution of hydrothermal fluids in the PACMANUS system, Manus Basin: The Sr and S isotope evidence. Geology 31 (9), 805–808.
Rouxel, O., Fouquet, Y., Ludden, J.N., 2004. Subsurface processes at the Lucky Strike hydrothermal field, Mid-Atlantic Ridge: Evidence from sulfur, selenium, and iron isotopes. Geochim. Cosmochim. Acta 68 (10), 2295–2311.
Rouxel, O., Ono, S., Alt, J., Rumble, D., Ludden, J., 2008. Sulfur isotope evidence for microbial sulfate reduction in altered oceanic basalts at ODP Site 801. Earth Planet. Sci. Lett. 268 (1–2), 110–123.
Sakai, H., Des Marais, D.J., Ueda, A., Moore, J.G., 1984. Concentrations and isotope ratios of carbon, nitrogen and sulfur in ocean-floor basalts. Geochim. Cosmochim. Acta 48 (12), 2433–2441.
Sauter, D., Cannat, M., Meyzen, C., Bezos, A., Patriat, P., Humler, E., Debayle, E., 2009. Propagation of a melting anomaly along the ultraslow Southwest Indian Ridge between 46°E and 52°20′E: Interaction with the Crozet hotspot? Geophys. J. Int. 179 (2), 687–699.
Sauter, D., Patriat, P., Rommevaux-Jestin, C., Cannat, M., Briais, A., 2001. The Southwest Indian Ridge between 49°15′E and 57°E: Focused accretion and magma redistribution. Earth Planet. Sci. Lett. 192 (3), 303–317.
Schwarzenbach, E.M., Gill, B.C., Gazel, E., Madrigal, P., 2016. Sulfur and carbon geochemistry of the Santa Elena peridotites: Comparing oceanic and continental processes during peridotite alteration. Lithos 252, 92–108.
Shanks III, W.C., Seyfried Jr, W.E., 1987. Stable isotope studies of vent fluids and chimney minerals, southern Juan de Fuca Ridge: Sodium metasomatism and seawater sulfate reduction. J. Geophys. Res. Atmos. 92 (B11), 11387–11399.
Shanks III, W.C., 2001. Stable isotopes in seafloor hydrothermal systems: Vent fluids, hydrothermal deposits, hydrothermal alteration, and microbial processes. Stable Isotope Geochem. 43, 469–525.
Shikazono, N., Kusakabe, M., 1999. Mineralogical characteristics and formation mechanism of sulfate-sulfide chimneys from Kuroko area, Mariana Trough and mid-ocean ridges. Resour. Geol., Special Issue 20, 1–11.
Stuart, F.M., Duckworth, R., Turner, G., Schofield, P.F., 1994. Helium and sulfur isotopes of sulfide minerals from middle valley, Northern Juan de Fuca Ridge. Proc. ODP Sci.

Results 139, 387–392.
Szynkiewicz, A., Moore, C.H., Glamoclija, M., Pratt, L.M., 2009. Sulfur isotope signatures in gypsiferous sediments of the Estancia and Tularosa Basins as indicators of sulfate sources, hydrological processes, and microbial activity. Geochim. Cosmochim. Acta 73 (20), 6162–6186.
Tao, C.H., Li, H.M., Huang, W., Han, X.Q., Wu, G.H., Su, X., Zhou, N., Lin, J., He, Y.H., Zhou, J.P., 2011. Mineralogical and geochemical features of sulfide chimneys from the 49 39′E hydrothermal field on the Southwest Indian Ridge and their geological inferences. Chin. Sci. Bull. 56 (26), 2828–2838.
Tao, C.H., Li, H.M., Jin, X.B., Zhou, J.P., Wu, T., He, Y.H., Deng, X.M., Gu, C.H., Zhang, G.Y., Liu, W.O., 2014. Seafloor hydrothermal activity and polymetallic sulfide exploration on the southwest Indian ridge. Chin. Sci. Bull. 59 (19), 2266–2276.
Tao, C.H., Lin, J., Guo, S.Q., John Chen, Y.S., Wu, G.H., Han, X.Q., German, C.R., Yoerger, D.R., Zhou, N., Li, H.M., Su, X., Zhu, J., 2012. First active hydrothermal vents on an ultraslow-spreading center: Southwest Indian Ridge. Geology 40 (1), 47–50.
Tivey, M.K., 2007. Generation of seafloor hydrothermal vent fluids and associated mineral deposits. Oceanography 20 (1), 50–65.
Wang, Y.J., Han, X.Q., Petersen, S., Jin, X.L., Qiu, Z.Y., Zhu, J.H., 2014. Mineralogy and geochemistry of hydrothermal precipitates from Kairei hydrothermal field, Central Indian Ridge. Mar. Geol. 354, 69–80.
Webber, A.P., Roberts, S., Murton, B.J., Hodgkinson, M.R., 2015. Geology, sulfide geochemistry and supercritical venting at the Beebe Hydrothermal Vent Field, Cayman Trough. Geochem., Geophy., Geosy. 16 (8), 2661–2678.
Woodruff, L.G., Shanks Iii, W.C., 1988. Sulfur isotope study of chimney minerals and vent fluids from 21°N, East Pacific Rise: Hydrothermal sulfur sources and disequilibrium sulfate reduction. J. Geophys. Res. Atmos. 93 (B5), 4562–4572.
Yang, W.F., Tao, C.H., Li, H.M., Liang, J., Liao, S.L., Long, J.P., Ma, Z.B., Wang, L.S., 2016. 230Th/238U dating of hydrothermal sulfides from Duanqiao hydrothermal field, Southwest Indian Ridge. Mar. Geophys. Res. 38, 1–13.
Yang, A.Y., Zhao, T.P., Zhou, M.F., Deng, X.G., 2017. Isotopically enriched N-MORB: a new geochemical signature of off-axis plume-ridge interaction-A case study at 50°28′E, Southwest Indian Ridge. J. Geophys. Res. 122 (1), 191–213.
Ye, J., Shi, X.F., Yang, Y.M., Li, N.S., Liu, J.H., Su, W.C., 2012. The occurrence of gold in hydrothermal sulfide at Southwest Indian ridge 49.6°E. Acta Oceanol. Sin. 31 (6), 72–82.
Zeng, Z.G., Jiang, F.Q., Qin, Y.S., Zhai, S.K., 2001. Sulfur isotopic composition of modern seafloor hydrothermal sediment and its geological significance. Acta Oceanol. Sin. 23 (3), 48–56 (In Chinese with English abstract).
Zeng, Z.G., Ma, Y., Chen, S., Selby, D., Wang, X.Y., Yin, X.B., 2017. Sulfur and lead isotopic compositions of massive sulfides from deep-sea hydrothermal systems: Implications for ore genesis and fluid circulation. Ore Geol. Rev. 87, 155–171.
Zhang, T., Lin, J., Gao, J.Y., 2013. Magmatism and tectonic processes in Area A hydrothermal vent on the Southwest Indian Ridge. Sci. China-Earth Sci. 56 (12), 2186–2197.
Zhou, H.Y., Dick, H.J.B., 2013. Thin crust as evidence for depleted mantle supporting the Marion Rise. Nature 494 (7436), 195–200.